Mechanical Engineering ETDs

Engineering ETDs

7-12-2014

Behavior of the Embedded Phase in a Shock-Driven Two-Phase Flow

Garrett Kuehner

Follow this and additional works at: https://digitalrepository.unm.edu/me_etds

Recommended Citation

Garrett M. Kuehner

Candidate

Mechanical Engineering

Department

This thesis is approved, and it is acceptable in quality and form
for publication:

Approved by the Thesis Committee:

Dr. C. Randall Truman, Chairperson

Dr. Peter Vorobieff

Dr. Alexander Korotkevich

Behavior of the Embedded Phase
in a Shock-Driven Two-Phase Flow

by

Garrett Munroe Kuehner

B.S., Mechanical Engineering, University of New Mexico 2012

THESIS

Submitted in Partial Fulfillment of the
Requirements for the Degree of

Master of Science
Mechanical Engineering

The University of New Mexico

Albuquerque, New Mexico

May, 2014

Dedication

To my family, for dealing with everything I threw at them.

"Above all, we must realize that no arsenal, or no weapon in the arsenals of the world, is so formidable as the will and moral courage of free men and women."

Ronald Reagan

Acknowledgments

Behavior of the Embedded Phase in a Shock-Driven Two-Phase Flow

by

Garrett Munroe Kuehner

B.S., Mechanical Engineering, University of New Mexico 2012
M.S., Mechanical Engineering, University of New Mexico, 2014

Abstract

This thesis presents an experimental study of droplet acceleration in a shock-driven two-phase flow. The study serves to identify the characteristics of the boundary layer growth behind a normal moving shock wave in a shock tunnel. Liquid propylene glycol droplets are pre-mixed with air, and slowly injected into the test section of the shock tunnel. Two test sections are evaluated during the course of this study. Each test section is constructed of square, transparent polycarbonate with internal cross section of 7.62 cm. The first test section contains features on the upper and lower surfaces of the test section, consistent with the holes used for the injection system during earlier Richtmyer-Meshkov Instability studies. The second test section has no surface features interfering with the flow, with smooth interfaces. The quiescent air seeded with propylene glycol droplets (diameter 0.5-3μm) is impulsively accelerated with a planar shock wave. A cross-section of the flow is illuminated with multiple pulses from Nd:YAG lasers, producing time-resolved visualizations of the seeded volume. The illuminated images are analyzed to quantify droplet velocity and vorticity from

time of shock passage to $400\mu s$ after shock. Velocity of the shock wave varies between Mach number 1.67 and 2.0. Based on Particle Image Velocimetry interrogation and analysis, a comparison is made between the velocity and vorticity fields in these two test sections..

Contents

List of Figures

Chapter 1

Introduction

1.1 Background of Shock Waves

A traveling wave is caused by a disturbance in a medium which propagates through its neighboring molecules [1]. The strength of the wave is defined by the amplitude of the disturbance. Strong waves with large amplitudes create large changes in the properties of the elastic medium the wave travels through. If the change in properties results in supersonic flow, the wave is categorized as a shock wave [1]. A shock wave is defined by John and Keith [2] as an infinitesimally thin region in a flow with discontinuous changes in fluid properties. The thickness of a shock wave is on the order of a mean molecular free path, roughly 10^{-5}cm. In this region, a large change in entropy occurs, largely due to the irreversibilities of friction between molecules of the medium [1]. The discontinuous, near immediate shift of a shock wave cause significant changes in fluid properties, i.e. pressure, velocity, temperature, flow direction, etc. [1, 2]. The instantaneous change in properties results from a transfer of kinetic and/or internal energy.

The orientation and motion of shock waves varies depending on the conditions of the upstream and downstream flow. Shock waves can occur both as traveling waves, and as standing waves. If the shock wave is not confined to a given space in the medium, it will transfer energy from one particle to another and move to areas of lower energy density [1, 2]. This pattern continues until the shock wave encounters an area of equal energy, commonly from another shock wave or a boundary with a different medium. This type of motion is a traveling wave. Conversely, if the energy of the medium upstream and downstream of the shock wave are equal, the shock wave remains stationary and is referred to as a standing wave [1].

Figure 1.1: A stationary shock wave forms on the wing of an aircraft, causing large flow deceleration and subsequent vapor condensation [3].

Typically for traveling waves, shock waves travel unidirectionally, from their source, either radially (in the case of high energy detonation caused by explosives [4]) or longitudinally if confined by an inelastic medium (as seen in shock tubes and supersonic wind tunnels [2]). Shock waves are not limited to a particular direction, and occur in many forms. Normal shock waves are defined as a shock wave acting perpendicular to the flow of the medium [1, 2]. However, if a shock wave is confronted by an inelastic medium or obstruction, the direction of the shock wave will reflect

and change. Shock waves which act at an angle to the flow of the medium are called oblique shocks [1].

Austrian physicist and philosopher Ernst Mach is credited as being the first scientist to recognize and document the reflection phenomena of shock waves, with documentation as early as 1878 [5]. Mach recorded two types of shock wave reflection configurations. His initial observation, a two shock wave configuration, is commonly called a regular reflection. Mach's second observation, a three-wave configuration, bears his name and is referred to as a Mach Reflection [5]. The focus of this thesis will be on singular, traveling normal shock waves.

Shock waves are of particular interest in a variety of fields. Such studies include, but are not limited to , detonation phenomena [4], transonic, supersonic and hypersonic vehicles and objects [6, 7], impulsively accelerated/decelerated flows [8], combustion characterization [4], and hypersonic air inlets [9].

1.2   Background on Boundary Layers

When considering real, practical fluid flow, fluid stress and viscosity must be given particular attention. Early attempts at defining fluid motion were first made by Swiss mathematician and physicist Leonhard Euler in 1757 [10]. In his article, General Principles of Fluid Motion, Euler published the general form of the continuity and momentum equations of fluid motion. These early equations are referred to today as the Euler inviscid equations of motion, as they do not define the transfer of stress between fluid particles. This simplified approach, although novel and groundbreaking for its time, could not determine cases of compressible, viscous fluid motion [10].

Viscosity plays an integral function in fluid motion and the phenomena asso-

ciated with it, particularly at the interface conditions of a fluid-solid boundary. On a quantum level, every particle or molecule of a fluid flow will have numerous collisions with other particles/molecules and with the solid boundary. These collisions will cause exchanges in kinetic and thermal energy, either from one particle to another, or from the particle to the surface. At the level of the surface, it is assumed that a fluid loses all of its momentum (e.g. velocity→0) in the interaction between the two, and that the fluid will exchange all thermal energy such that the temperature of the fluid and the surface will be the same [11].

The assumption that the velocity of the fluid relative to the surface is zero is often called the no-slip condition [11, 1, 2, 10]. This assumption defines the surface as a sink for fluid momentum. Far from the surface, the fluid velocity is considered free-stream, where the velocity is greatest. The transition area from zero velocity at the surface to 99 percent of free stream velocity is defined as δ, the boundary layer height [11].
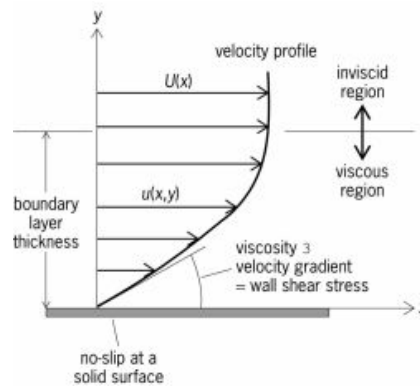
Figure 1.2: Boundary-layer profile of a fluid flow over a flat plate. The image also depicts the regions of viscous and inviscid flow [12].

In the 19th Century, French physicist Claude-Louis Navier and Irish physicist Sir George Stokes continued with Euler's early approximation by applying Newtons

second law of physics to fluid motion, along with the assumption that fluid stress is the summation of a diffusive viscous term and a pressure term [10]. These additions complemented Euler's early work, and allowed for the direct calculation of compressible and viscous fluid motion. These complete solutions are known as the Navier-Stokes equations [10].

Although the Navier-Stokes equations completely defined fluid motion, they were mostly left unused for half a century. These equations are nonlinear, partial differential equations, which are difficult to compute even by modern standards. For this reason, early application of the Navier-Stokes equations led to great simplifications to ease computation, which practically reversed them to the initial inviscid Euler equations. With simplification of the Navier-Stokes equations, the order of the system is reduced from second to first order. When solving the first order system, only one boundary condition could be imposed either the boundary layer to solid surface interface, where fluid velocity with respect to the surface velocity are equal, or the boundary layer to free stream velocity, which must also be equal. Neglecting the no-slip condition led to zero wall shear stress, and the Eulerian inviscid flow analysis [10].

In 1904, German engineer Ludwig Prandtl reasoned that flows of high Reynolds number would result in a thin region of fluid flow near the surface where viscous effects would act. This region of high variation between free stream and zero relative velocity would produce large gradients and significant shear forces, due to Stokes relation of shear stress to fluid viscosity and velocity gradient [11, 10]. Although the region was significantly smaller than the volume of total flow, it could not be ignored since all transfer of heat and momentum occurs within the region. Prandtl reasoned that flow outside the boundary layer area behaved as an inviscid fluid. To attain this numerically, Prandtl separated the two regions for computational purposes. Since

the outer region behaved without viscous effects, Prandtl used the inviscid Euler equations. The inner boundary layer region followed the Navier-Stokes equations with simplifications assumed. Prandtl is credited with the modern interpretation of the boundary layer concept for his computational work with the Euler and Navier-Stokes equations [10].

1.3 Governing Equations

1.3.1 Normal Shock Waves

The behavior and characteristics of a standing shock wave are defined from Zucker and Biblarz [1]. Starting with the equation of continuity and substituting density for the ideal gas equation of state as well as the velocity yields:

$$\frac{p_1 M_1}{\sqrt{T_1}} = \frac{p_2 M_2}{\sqrt{T_2}} \tag{1.1}$$

Following a similar method, an energy (enthalpy) balance can be created. However, since it is assumed that gas at relatively low pressure and high temperature behaves as an ideal gas, enthalpy is simplified to be a function of temperature. Treating the specific heat of air to be constant under these conditions yields:

$$T_1 \left(1 + \frac{\gamma - 1}{2} M_1^2\right) = T_2 \left(1 + \frac{\gamma - 1}{2} M_2^2\right) \tag{1.2}$$

Substituting density and velocity of a perfect gas into the momentum equation for an arbitrary fluid yields:

$$P_1 \left(1 + \gamma M_1^2\right) = P_2 \left(1 + \gamma M_2^2\right) \tag{1.3}$$

Where p, M, T are the state variables of pressure, Mach number and Temperature, and γ is the ideal specific heat ratio. It should be noted that the above equations were

derived for standing normal waves. The extent of this study will focus on traveling normal waves. To this end, a uniform velocity must be superimposed to use the steady flow equations. Since these equations are used to evaluate the thermodynamic state of the medium before and after a shock, they are not concerned with the transience associated with the transfer of energy from the shock. The velocity superposition does not affect the static thermodynamic state, but does alter the stagnation pressure, which will not be considered in this study.

Manipulation of equations (1.1-1.3) gives the pressure ratio in terms of the specific heat and the Mach Numbers before and after shock passage:

$$\frac{p_1}{p_2} = \frac{1 + \gamma M_2^2}{1 + \gamma M_1^2} \tag{1.4}$$

Further substitution of equations (1.1-1.3) into (1.4) yields the post-shock Mach Number in terms of the preshock Mach number and the specific heat ratio:

$$M_2^2 = \frac{M_1^2 + \dfrac{2}{\gamma - 1}}{\dfrac{2\gamma}{\gamma - 1} M_1^2 - 1} \tag{1.5}$$

Equation (1.5) above is solely dependent on the pre-shock Mach Number and the specific heat ratio. Using this relationship and substituting it into equation (1.4) disassociates the dependence of the pressure ratio on M_2.

$$\frac{p_2}{p_1} = \frac{2\gamma}{\gamma + 1} M_1^2 - \frac{\gamma - 1}{\gamma + 1} \tag{1.6}$$

Similarly, combining the previous two equations forms the density ratio, which is also dependent on M_1 and γ:

$$\frac{\rho_2}{\rho_1} = \frac{(\gamma + 1)M_1^2}{(\gamma - 1)M_1^2 + 2} \tag{1.7}$$

To reiterate, the equations derived above are applicable only to perfect (ideal) gases. Although the pressure ratio and temperature range of the experiments is such that

the quiescent air undergoing shock acceleration can be considered a perfect gas, the addition of liquid glycol droplets as tracer particles cannot be considered ideal.

As the glycol particles transition from near-zero velocity suspension in the stationary air to an accelerated state after shock passage, the particles are large and dense enough to affect the flow characteristics of the air around them, and subsequently, the boundary layer growth behind the shock wave. Elghobashi studied this particular transport phenomena, the dispersion of particles in turbulent shear flows [13]. The characterization of the phenomena requires the understanding of two-way nonlinear coupling. In one respect, the particles are reacting to the turbulent fluid flow around them. On the other hand, the particle acceleration requires enough energy from the flow, such that the particle motion affects the frequency of the turbulence [13].

Elghobashi quantified this coupling motion through computational dynamic simulation [13]. His results showed that the coupling, and thus the effect of the seeded tracer particles on a fluid flow, is directly proportional to the size and mass of the particles, and the volume fraction the particles encompass (also referred to as the state of suspension). Dilute suspensions define a low, or diluted, volume fraction of the particle concentration, while dense suspensions define a flow with heavily concentrated particles. To describe this dependence, Elghobashi created varying states of coupling. One-way coupling defines the state where the particle motion is dependent on the turbulence of the fluid flow, but with little to no effect of the particles disturbing the turbulent structures. Two-way coupling denotes the relationship where particle concentration tends to affect the fluid flow. In four-way coupling, the volume fraction has reached a state of dense suspension, enough to cause particle-particle collisions [13]. The effects of particle concentration on the experiments conducted in this study will be evaluated further in Chapter 4.

1.3.2 Boundary Layers

As mentioned previously in Section 1.1, Ludwig Prandtl is recognized for his analytical work on defining the governing equations for a boundary layer [10]. Starting with the two dimensional, incompressible Navier-Stokes equations, and introducing scaled variables $U = \dfrac{u}{U_\infty}$, $V = \dfrac{v}{V_\infty}$, $X = \dfrac{x}{L}$, $Y = \dfrac{y}{L}$, $P = \dfrac{p}{\rho_{ref}U_\infty^2}$, and $\mu = \dfrac{u}{\mu_{ref}}$:

$$\frac{\partial U}{\partial X} + \frac{\partial V}{\partial Y} = 0 \tag{1.8}$$

$$U\frac{\partial U}{\partial X} + V\frac{\partial U}{\partial Y} = -\frac{\partial P}{\partial X} + \frac{1}{Re}\left(\frac{\partial^2 U}{\partial X^2} + \frac{\partial^2 U}{\partial Y^2}\right) \tag{1.9}$$

$$U\frac{\partial V}{\partial X} + V\frac{\partial V}{\partial Y} = -\frac{\partial P}{\partial Y} + \frac{1}{Re}\left(\frac{\partial^2 V}{\partial X^2} + \frac{\partial^2 V}{\partial Y^2}\right) \tag{1.10}$$

Where

$$Re = \rho_{ref}U_\infty\frac{L}{\mu_{ref}} \tag{1.11}$$

For large velocities in the U direction, the Reynolds number increases, thus driving the right hand terms to become negligible. Consequently, the viscosity disappears from the system (resulting in zero momentum and thermal energy transfer to the boundary), and the system order is reduced by one. The result of the solution to this oversimplification is a singular required boundary condition, rather than two. The no-slip condition in the boundary layer and the continuity between the boundary layer and the free stream flow cannot be held simultaneously.

Prandtl evaluated the system of equations as the highest order derivative approaches zero by introducing a second order model problem, similar to a spring-mass-damper system.

$$m\frac{d^2x}{dt^2} + a\frac{dx}{dt} + cx = 0 \tag{1.12}$$

with exact solution

$$x(t) = C_1 e^{\lambda_1 t} + C_2 e^{\lambda_2 t} \tag{1.13}$$

where $\lambda_{1,2}$ are the eigenvalues of the solution and have discrete solutions of

$$\lambda_{1,2} = \frac{-a \pm \sqrt{a^2 4mc}}{2m} \tag{1.14}$$

As the m coefficient approaches zero, the solution of x(t) becomes

$$x(t) = C_2 e^{-\frac{c}{a}t} \tag{1.15}$$

Similarly, if a new independent variable $\zeta = $ t/m is introduced to the spring-mass damper system, the equation becomes

$$\frac{d^2x}{d\zeta^2} + a\frac{dx}{d\zeta} + mcx = 0 \tag{1.16}$$

By introducing ζ, the transformation effectively stretches the thin boundary layer region near t $= 0$, where rapid changes in x(t) can occur for relatively small values of m. As m approaches zero, the system remains a second order system, enabling the use of two boundary conditions. The solution to the two regions of the flow are:

$$x_{inner}(t) = \frac{m}{a}\left(1 - e^{-\frac{a}{m}t}\right) \qquad x_{outer}(t) = \frac{m}{a}e^{-\frac{c}{a}t} \tag{1.17}$$

Following the same variable stretching to the normal coordinate Y and velocity V to the Navier Stokes Equation, and imposing the no-slip and continuity boundary conditions on the scaled normal coordinate ($y^*(0) = 0$, $y^*(\infty) \Rightarrow \infty$). The resulting Navier-Stokes equations for a boundary layer are:

$$\frac{\partial u}{\partial x} + \frac{\partial v}{\partial y} = 0 \tag{1.18}$$

$$u\frac{\partial u}{\partial x} + v\frac{\partial u}{\partial y} = -\frac{1}{\rho}\frac{\partial p}{\partial x} + \nu\frac{\partial^2 u}{\partial y^2} \tag{1.19}$$

$$\frac{\partial p}{\partial y} \approx 0 \tag{1.20}$$

Note the significance of the third equation, which states that the pressure differential in the normal direction to flow is zero. This complements Prandtl's assumption, that for a boundary layer the pressure across the boundary and into the fully developed flow is constant [10].

1.4 Shock Wave-Boundary Layer Interaction

Given the nature of this study, the effect of a shock wave on a boundary layer should be given considerable thought. A shock wave-boundary layer interaction (SBLI) can occur on internal and external flows, with a vast variety of structure complexity. At the instant of interaction, the boundary layer is subject to an instantaneous step in entropy from the shock wave, introducing an adverse pressure gradient. Initially, the higher pressure can compress the boundary layer, causing it to shrink. Afterward, however, the boundary layer profile becomes distorted, causing it to become less full. Ultimately, the boundary layer expands, influencing the neighboring inviscid flow to the point of complete flow separation. Alternatively, the shock must react to a multilayered viscous and inviscid flow structure [7].

Shock wave-boundary layer interactions occur when a shock wave converges with a boundary layer. In a transonic flow and larger, such interactions are commonplace. As a result, SBLIs are a principal topic of research in a multitude of areas, experimentally and computationally. Common areas of SBLI research are transonic, supersonic and hypersonic wings and air inlets, fuel-air mixing in scramjet combustion, gas-turbine engines, etc.. Weiss and Oliver [9], and Chyu, Rimlinger and Shih [14] have performed studies on shock wave-boundary layer interaction, specifically on controlling the onset of flow separation through the use of bleeds and normal slot suction. The physical characteristics of the bleed and normal slot mimic the experimental setup used in this study, which will be discussed in Chapter 3. Both studies proved that the calculated use of bleeds and normal suction slots can reduce the onset of flow separation, enough to cause the collapse of an oblique shock train into a single normal shock [9] or to maintain a uniform boundary layer after shock passage [14].

However useful SBLIs are in a wide array of studies, they will not be useful for

this particular study. The defining characteristic of SBLI research is the onset of a shock wave to a pre-existing boundary layer. A pre-existing boundary layer requires an initial flow to cause a no-slip condition near the fluid-solid border. For this study, a volume of air premixed with glycol droplets as tracer particles is initially at rest, then accelerated from a normal shock passage. Since the volume is initially at rest, there is no velocity gradient, and therefore no initial boundary layer. The focus of this study will be the growth of the boundary layer after time of shock passage.

1.5 Goals of Study

The objective of the work presented in this study is to quantitatively assess the boundary layer growth rate behind a traveling normal shock. Recent work by Anderson [15], White [16], and Olmstead et al. [17] in the study of Richtmyer-Meshkov Instability growth of a seeded dense gas column interface with normal and oblique traveling shock waves has illuminated certain flow behavior within the boundary layer at the upper and lower boundaries of the shock tube. Although some theories exist which could explain the flow behavior, no quantitative experiments have been conducted as of yet to fully ascertain the source for these behaviors. It is the intention of this study to conclusively provide the reason for this phenomenon.

Chapter 2

Early Work on Shock Wave-Boundary Layer Interaction

The study of boundary layer growth behind a shock wave has been limited to normal shock waves occuring within a shock tube. Early work in this area began in the 1950s, and has expanded over the past 60 years. The focus of early studies was primarily limited to experimental investigations. However, the advent of computers and decreased computation time since this period has generated more numerical investigations into shock wave boundary layer interaction. The experiments explained in this thesis have been performed in a shock tube for an initially unperturbed, quiescent volume of air.

2.1 Boundary Layer growth behind Traveling Normal Shock Wave

Following World War II, the topic of supersonic fluid interactions became of particular interest. First, a supersonic shock following an atomic explosion and the effects

of the shock were of particular interest. Second, the advent of high speed rockets following the war necessitated a knowledge of supersonic aerodynamics, in particular, supersonic boundary layers. A pioneer in this field of study was Harold Mirels, who conducted a majority of the studies reviewed herein.

In 1955, Mirels produced his early analytical work [18] on the growth of a boundary layer behind a shock wave at the Lewis Flight Propulsion Laboratory in Ohio for the National Advisory Committee for Aeronautics (NACA). Early publications provided equations for the growth of laminar and turbulent boundary layers behind a traveling shock wave. Mirels assumed the shock wave traveled with constant velocity into a stationary fluid. For the turbulent boundary layer, integral methods were used by extending empirical data obtained for a semi-infinite flat plate. For simplicity, a $\frac{1}{7}$ power law was used for the velocity profile relative to the wall [18, 19]. Mirels's equations can be found in Appendices A and B. To use Mirels's equations for turbulent flows, an expression for the skin friction must be imposed. Mirels used the Blasius relation, which is defined for incompressible flow. The Blasius relation was extended to compressible flow using a mean temperature T_m to define the average fluid properties, shown in Appendix B [18, 19]. Since Mirels published NACA TN-3712, many studies have been conducted which validate his general approach to laminar and turbulent boundary layers [20, 21, 22, 23].

In 1957, Mirels published another document on boundary layers, NACA TN 1333 [24]. In the report, Mirels explains the 4 regions of a shock tube during an experiment in stationary air, and the effect of the boundary layer on attenuation of the traveling shock. At the onset of an experiment, when the driver gas is released (typically via diaphragm rupture) into the stationary driven gas, a shock wave propagates into region 1, while an expansion wave propagates into region 4 [24]. Region 1 consists of the stationary air, before acceleration due to the shock front, and is

separated from region 2 by the normal shock wave. Region 2 is the accelerated air behind the shock front, where a boundary layer forms due to viscous effects at the walls of the shock tube. Region 2 is separated from region 3 by the 'contact surface', which is the contact between the driven gas (air) and the driver gas (in Mirels' experiments, compressed air). Region 3 consists of the driver gas (compressed air) traveling downstream behind the contact surface and accelerated air. Region 3 travels slower than the normal shock wave, and slower than the accelerated air in region 2. For this reason, the boundary layer height in region 3 is smaller than the boundary layer in region 2. Region 4 is also compressed air, but has not started to expand downstream and therefore has no velocity. Regions 3 and 4 are separated by expansion waves. Mirels derived equations to express the generation of waves by unsteady boundary layer action, which occur as either compression or expansion waves normal to the velocity profile. In region 2, the boundary layer growth induces expansion waves, which attenuate the initial normal shock, while the boundary layer in region 3 induces compression waves, which accelerate the shock. Mirels conducted experiments in a $\frac{1}{6}$ by $\frac{1}{8}$ foot rectangular cross section high-pressure air-air shock tube, and confirmed his analytical theory [24].

In 1964, Mirels provided an analytical investigation of test time limitation due to premature arrival of contact surface for wholly-turbulent boundary layers [25]. Contrary to his previous work, Mirels argued that the traveling shock wave in a shock tube does not travel at constant velocity. Rather, he claimed that viscous effects cause the shock wave to slow and the contact surface to accelerate, resulting in reduction of separation distance between the interfaces of regions 1-2 and 2-3. At the limit of this reduction of separation distance, contact surface and shock move at the same velocity. Mirels numerically quantified that the limiting separation distance is met when mass flow entering the shock equals the boundary layer mass flow moving past the contact surface. Mirels concluded that the separating distance of turbulent boundary layers

is less sensitive to variations in diameter and pressure than laminar cases [25].

Using Mirels' laminar [26] and turbulent [27] approximations for boundary layer growth, the following graphs were made.

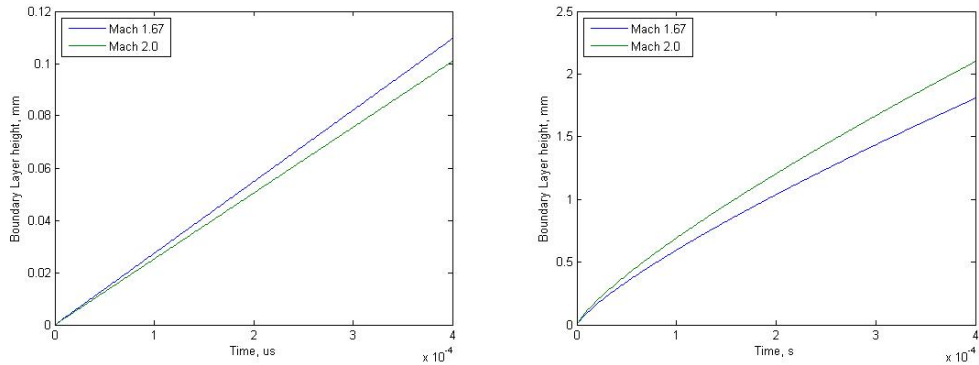Figure 2.1: The image on the left shows the laminar growth profile according to Mirels. On the right is the turbulent growth profile according to Mirels.

For good measure, the Reynolds number was also plotted for Mach numbers 1.67 and 2.0 vs time over a semi-infinite plate. As the shock moves downstream, the length of the plate 'grows', causing a change in the characteristic length, and thus increasing the Reynolds number linearly.
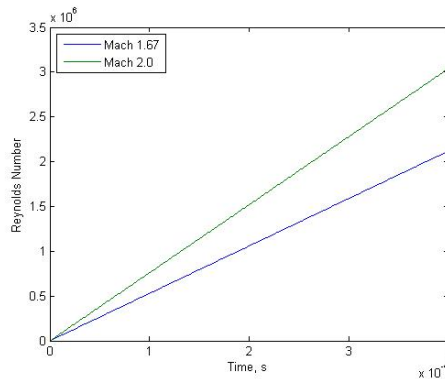
Figure 2.2: Reynolds Number vs Time for flow over semi-infinite flat plate

In 1977, Raymond Brun et al. [8] conducted experiments to characterize the transition from laminar to turbulent flow in a shock tube wall boundary layer. Empirical measurements were made with 5 thin film platinum gauges deposited on glass and flush mounted at the wall surface. From the gauges, wall temperature and corresponding heat flux were measured and deduced. The variation in the gauge resistance with a constant current source led to oscilloscope readings with clear indication of the shock passage through the driven gas (argon), the transition of the boundary layer, the contact surface of the driver gas (nitrogen, helium and hydrogen) and eventually the reflected shock wave. It was determined that the stability regime is a function of the shock Mach number, and the initial pressure. The measurements of Brun et al. correspond to previous results of Mirels [25], where the boundary layer is stable for values of the product of initial pressure and hydraulic diameter less than 0.5 in.cm Hg. It was also determined that the creation of pertubations occur at consistent time intervals, and that any perturbation is transported in the boundary layer with a velocity nearly equal to that of the free stream [8].

In 1996, V.M. Boiko et al. [28] produced an experimental and theoretical investigation of shock wave propagation into a two-phase region. Their research

consisted of a controlled deposition of varying types of particles, (acrylic, $80\pm 300\mu$ m, $\rho =$1.2g/cm^3; bronze, $80\pm 130\mu$ m, $\rho =$8.6g/cm^3), with varying deposition densities (0.2% and 3%) and shock velocities (Ma = 1.5 - 4.5) [28]. Particle deposition was carried out by two methods. First, an electromagnetic propulsion device on the lower wall of the shock tube measurement section accelerated the particles upwards to a required height, whereupon the passing shock front would pass through the particles at a precise time. Second, a vibrating grid on the upper lid of the measurement section would create a uniform cascading vertical flow of free falling particles over the cross section. Visualization was performed by multiframe shadow visualization and scattered laser light methods. Results indicated that particles become separated by size following shock acceleration due to faster acceleration of smaller particles than larger particles. Particle acceleration also differed by a factor of 2 from concentrations varying between 0.1% and 1%. The wave structure of the reflected shocks of each particle overlap more frequently for higher concentrations of particle clouds, and form a collective leading shock. This realization concurs with the work of Elghobashi et al. [13], and his description of two-way and four-way coupling. Boiko et al. [28] concluded that a compression wave arises in the cloud of particles due to the deceleration of the gas, and the compression wave is transformed into a shock wave which moves toward the gas flow. This shock wave leaves the cloud of particles, accelerating the gas flow [28].

In 2003, Petersen and Hanson [19] revisited Mirels' original analytical work [18] on the boundary layer growth behind a normal shock. Petersen and Hanson used the same boundary layer equations as Mirels proposed in 1955, but did not complete the model with the Blasius wall friction expression. Since the Blasius friction expression was originally for incompressible flow and then expanded to include compressible flow by using a mean temperature to define average fluid properties, the Spalding Chi and Van Driest II skin friction correlations were used for comparison. For turbulent

flows, the Blasius skin friction correlation is much smaller smaller (50-100%) than either the Van Driest II or Spalding Chi correlations. The Spalding Chi and Van Driest II converge for highly turbulent flows ($Re = 10^8$), with the Spalding-Chi skin friction being smaller for laminar flows. The new model for boundary layer growth is nearly identical for low pressure (P = 1atm), but varies by 30% and 66% for 50atm and 500atm, respectively. The new model is particularly useful in high pressure shock tubes where larger Reynolds numbers lead to early boundary-layer transition to turbulence. Overall, it was concluded that nonidealities caused by viscous effects are expected to be greater in high-pressure shock tubes [19].

In 2005, Suzuki et al. [29] conducted shock tube experiments to clarify the mechanism responsible for dust entrainment behind a planar shock wave. Their experiments used pressurized air to inject a single particle (0.3-5.57mm) into the test section before diaphragm rupture. The planar shock wave reached the particle at the apogee of particle flight ($v_y = 0$), while the particle was positioned in the center of the shock tube. Drag Coefficient measurements of the accelerating spherical particle were deduced from mean velocity and acceleration. Suzuki et al. also conducted a second experiment where the particle was placed at rest on the bottom of the test section, and the test section surface roughness was varied [29]. Translational velocity and rotational speeds of the second experiment were measured to quantify mechanisms of entrainment. Suzuki et al. found that the drag coefficients of the particles were roughly 20% higher than those derived from standard drag curve, and that floor conditions affect linear velocity and rotational speed of particles. It was concluded that particle rotation is not an effective mechanism for particle lift-up and entrainment in a passing flow. Rather, it was speculated that the upward forces on particles are due to shock reflections on floor, with higher surface roughness causing more oblique shock reflections [29].

In 2012, Wagner et al. [30] at Sandia National Laboratories reassessed the historical drag coefficient data for spherical particles in shock-induced flows from a traveling normal shock wave, similar to the work previously mentioned by Suzuki et al. in 2005 [29]. Their study tracked the trajectories of 1-mm spheres at varying Mach numbers, specifically Ma=1.68, 1.93, and 2.04 through a Schlieren imaging system and particle tracking velocimetry (PTV). Wall boundary layer growth and particle-particle interactions were eliminated through their particle injection system, which utilized a linear motor and push rods to precisely deposit a limited number of 1mm spheres into the test section. The planar shock wave reached the particles as they fell due to gravity through the test section, with careful timing to ensure the particle(s) remained outside the wall boundary layer. Their research confirmed the work of Suzuki et al., where drag increases with increased Mach number, and also exceeded values predicted by incompressible drag models. Compressible drag models of Loth [31] and Parmar et al. [32] coincide very closely to experimental results of Wagner et al.. The results of Wagner et al. indicate unsteadiness should not be expected to contribute to drag increase over long time scales of experiments, rather their observations suggest elevated particle drag coefficients are quasi-steady phenomena attributed to increased compressibility rather than true flow unsteadiness [30].

2.2 Post Shock Boundary Layer growth of steady fluid flows

Although this particular thesis does not focus on steady (constant) fluid flows, much information can be derived from their area of study, particularly in the area of reflected shock wave interaction with a boundary layer.

In 1995, Chyu et al. [14] conducted a numerical investigation of bleed effectiveness in controlling shock wave-boundary layer interaction on flat plate. The numerical processes utilized in their study included fully compressible Navier-Stokes equations closed by a Baldwin-Lomax model with solutions obtained by implicit finite volume method on an overlapping grid. Particular attention was paid to the effects of bleed-hole angle, the presence of upstream and downstream bleed holes, and pressure ratio across bleed holes effects on the structure of a barrier shock, surface pressure distribution, and bleed rate. Their computations included bleed holes, very similar to the injection holes used in this thesis, with varying angles between 30° and 90° to flow. Their study found that the interaction of the passing normal shock and the bleed holes caused two different types of barrier shocks; Prandtl-Meyer expansion waves at the leading (upstream) edge of the bleed hole, and a reflected barrier shock at the trailing (downstream) edge [14]. The presence of these two barrier shocks affect the boundary layer growth, causing the fluid velocity after the bleed site to decrease significantly, as shown in figure 2.3. This decrease in flow velocity causes a significant increase in the boundary layer height.
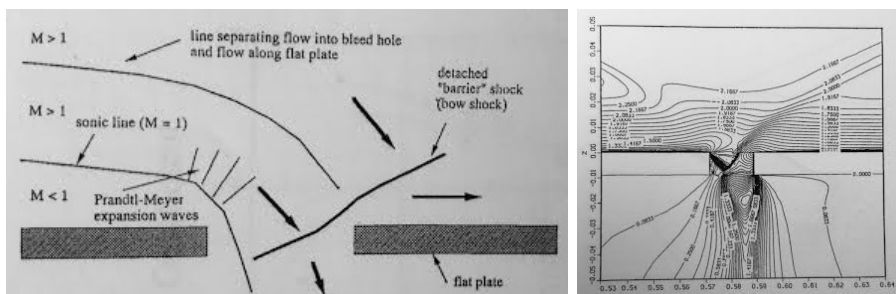

Figure 2.3: The image on the left shows Chyu's et al. [14] study on the development of expansion waves and barrier shocks from the redirection of flow out of a bleed. The image on the right shows the resulting Mach number contours from the redirection of flow. Note the rapid growth of the boundary layer after the bleed slot in the image on the right.

In 2011, Weiss and Olivier [9] conducted experiments to quantify the behavior of a shock train with a normal suction slot in a diverging half angle (1.5°) shock tube. The Reynolds numbers of the flow were varied; and the structure and pressure recovery within the shock train was analyzed by means of Schlieren images and wall pressure measurements with boundary layer measurements taken from a pitot probe. Their results discovered when pressure in the suction slot is smaller or equal to the static pressure of the incoming supersonic flow, the pressure gradient across the primary shock is sufficient to push some part of the near wall boundary layer through the suction slot. Due to the suction stabilized primary shock foot, the back pressure of the shock train can be increased until the shock train gradually changes into a single normal shock. From further manipulation of the pressure in the suction slot, the single normal shock could be moved up and downstream, resulting in a standing normal shock at a desired location [9].

2.3 Previous Work at the University of New Mexico

Since 2007, the University of New Mexico shock tube facility has studied fluid instabilities induced by transonic and supersonic shock accelerated flows. In particular, the focus at UNM has been on Richtmyer-Meshkov Instabilty (RMI), Kelvin-Helmholtz Instability (KHI), and particle lag instability (PLI) from supersonic shock acceleration. The research conducted in these areas has spurned some questions regarding the results discovered, and it is the intention of this thesis to study and characterize certain behaviors witnessed.

In 2011, White [16]conducted an experimental study on Richtmyer-Meshkov instability due to an oblique interaction of a cylindrical gas column seeded with

glycol droplets. A column of Sulfer Hexafluoride (SF_6) seeded with glycol droplets was injected into the test section of the UNM shock tube by means of an injection hole through the test section. The gas flow was stabilized through a co-flow of air around the column and the oblique shock interaction was created by inclining the shock tube to 15°, while the SF_6 remained vertical. Experiments were conducted with a shock Mach number of 1.67. Visualization was achieved by 532nm Nd:YAG lasers, and image capture from an Apogee Alta U42 high performance cooled CCD camera. Visualization of the accelerated gas column was conducted in the horizontal and vertical plane,as shown in Figure 2.4. The study investigated the morphology of the Richtmyer-Meshkov instability and particle lag instability, with attention to the effect of the injection holes through the test section on instability growth [16].
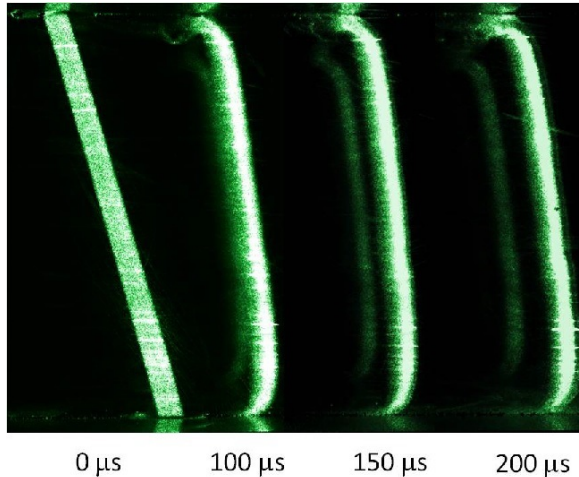
Figure 2.4: PLIF images of a column of SF_6 gas accelerated by an oblique shock over time [16, 15]. As time after shock increases, the column accelerates to piston velocity, and deforms in the process. The column velocity slows at the fluid-solid interfaces at the upper and lower bounds of the time series images, shown by the curvature of the column in these locations.

Figure 2.4 shows interesting features of the boundary layer. As expected, the gas column accelerates in the streamwise direction following shock impact, with

viscous effects slowing the acceleration at the upper and lower bounds of the test section. It is assumed the areas near the upper and lower bounds where the column has slowed is the boundary layer, where flow velocity is less than 99% of free stream velocity. A boundary layer is to be expected in a flow such as this; however the magnitude of the boundary layer is much higher than anticipated. According to Mirels [18], the boundary layer height for early timings such as these should be near 1mm. For the 76.2mm test section used in these experiments, the boundary layer is nearly 10mm, a full order of magnitude higher than Mirels predicted.

Also in 2011 at the University of New Mexico, Anderson [15] conducted an experimental and numerical investigation of instabilities formed by the interaction of a planar shock wave and a cylindrical column of SF_6 gas seeded with glycol droplets. The investigation followed the work of White [16], and was intended to draw conclusions between experimental observations and numerical analysis. Numerical analysis was performed using the Eulerian hydrodynamics code SHAMRC (Second-order Hydrodynamic Automatic Mesh Refinement Code). The numerical results closely coincided with those witnessed experimentally, shown in Figure 2.5 [15], although the boundary layer height is much smaller than found experimentally.
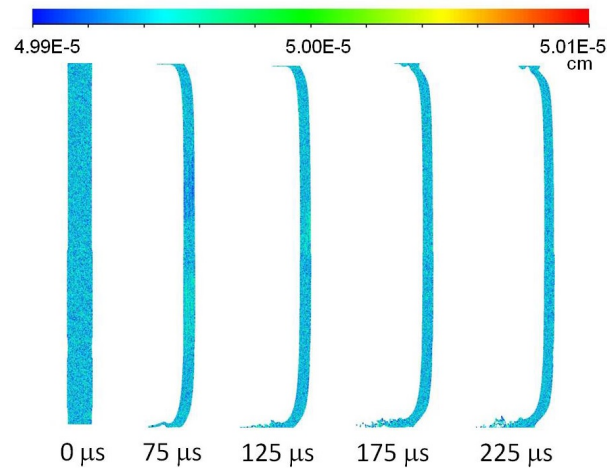
Figure 2.5: Computational modeling of a shock accelerated gas column from Anderson's dissertation [15]. The column lags at the fluid-solid interface, consistent with experimental analyses, although significantly less.

Anderson also questioned the impact of injection holes in the test section on the flow at the wall boundaries [15]. Included in his numerical study was the planar shock interaction with a gas column, but with the injection holes removed from the model. As this is only possible to do numerically and maintain a perfect column of gas, the experimental study cannot be reproduced.
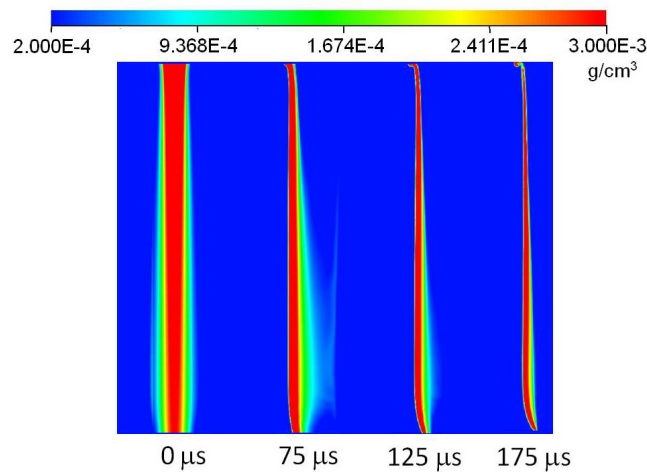
Figure 2.6: Computational modeling of a shock accelerated gas column performed without the effects of the injection holes [15].

Shown in Figure 2.6, the top of the column remains nearly straight, with a very small instability that forms at 175 μs. At the bottom of the shock tube, the column bends in the opposite direction as observed in Figure 2.6 for the multi-phase instability. Anderson postulated the bend is caused by the variation in the density near the bottom of the column, a feature that is not present in the multi-phase case. When the holes are included in the calculation, this variation in density cancels out the deceleration caused by the locally lower shock pressure. The result is a column that appears to have a both a backward and forward bend at later times [15].

In 2013 at the American Physical Society Division of Fluid Dynamics Annual Meeting, Olmstead et al. [17] from the University of New Mexico presented on the three-dimensional features of RMI caused by shock-driven mixing flow. Their research increased the breadth of previous works of White [16] and Anderson [15] for a range of an oblique shock wave Mach numbers (1.2 to 2.0) across a cylindrical column of SF_6 in air. Image capturing was performed using Planar Laser Induced Fluorescence (PLIF) rather than visible laser exposure previously utilized. Images were obtained

in multiple planes along and across the RMI-perturbed column for horizontal, 15°
and 30° oblique shocks by inclining the shock tube while the gas column remained
vertical. The main subject of the investigation was the effect of the angle between the
cylinder and the shock front in the formation and evolution of the three-dimensional
features in the flow [17].
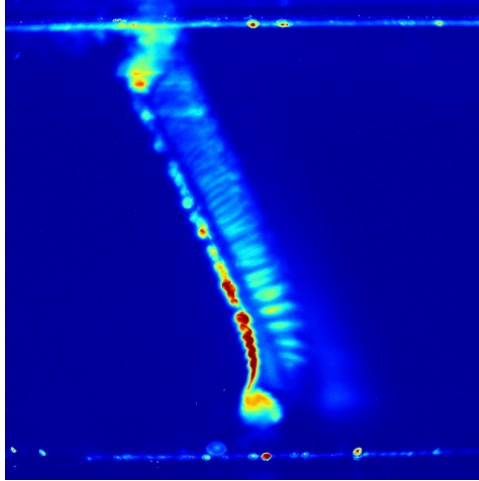
Figure 2.7: Olmstead et al. image of Oblique Shock Interaction with Gas Column
[17].

2.4   Motivation for Study

The intention of this thesis is to quantitatively analyze the boundary layer growth of a
multiphase flow (air and glycol droplets) in the UNM shock tube facility. The results
witnessed from the previously mentioned work [16, 15, 17] indicate the boundary layer
growth for the shock accelerated gas column is much higher than predicted by Mirels
[18, 25].

In this thesis, the boundary layer growth will be analyzed for a smooth test
section, devoid of the injection holes used for the RMI accelerated gas column studies,

for Mach numbers 1.67 and 2.0 from time of shock passage to 400μs after shock. Flow visualization will be performed by depositing glycol droplets inside the test section, and exposing the test section with 2 532nm Nd:YAG double pulsed lasers. The test section will then be removed, and replaced with the same test section used in the accelerated gas column studies with the 90° injection holes at the upper and lower surfaces. Camera placement will remain over the hole for all images.

Chapter 3

Experiment Setup

The experimental data presented in this thesis was gathered using the University of New Mexico (UNM) shock tube facility. The facility was constructed in 2007-2009 with funding provided by the Defense Threat Reduction Agency (DTRA). Since completion, the facility has continued to be funded by DTRA, the National Nuclear Security Administration (NNSA) and National Science Foundation (NSF). The UNM shock tube facility (aka laboratory) has been used to gather experimental data to better understand fluid dynamic instabilities and phenomena, including but not limited to Kelvin-Helmholtz Instability (KHI), Richtmyer-Meshkov Instability (RMI), and boundary layer growth behind normal and oblique shock waves. This particular study focuses on the boundary layer growth behind a normal shock wave in the absence and presence of a flow diverting feature. The following chapter provides a synopsis of the facility and equipment used to gather the data used in this study.

3.1   Shock Tube

The shock tube at the University of New Mexico consists of four modular sections: the driver, the driven, the test, and the run-off sections, as shown in Fig. 3.1. The driver section is separated from the driven section initially, allowing for the driver section to be pressurized independent of the other three sections. During an experimental test, or run, the separating diaphragm is ruptured, allowing the pressurized driver gas to travel downstream through the driven, test, and runoff sections. During supersonic flows, a shock wave forms in front of the driver gas within the driven section, which propagates into the test section and causes the initial conditions in the test section to be exposed to an adverse pressure gradient. This pressure gradient accelerates the initial conditions, and is captured through high speed photography and light exposure.
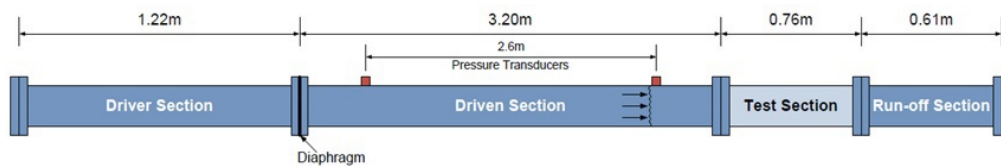
Figure 3.1: Schematic of UNM Shock Tube.

The mounting orientation of the shock tube assembly is inclinable, varying from the horizontal position at 0 degrees to an inclined 45 degree position with infinite settings in between. Historically, data gathered in the inclined position has been at 15 and 30 degrees [15, 17], and not until recently has an incline of 45 degrees been achievable. The purpose of inclining the test section is to produce oblique shock waves with respect to the initial conditions. In the horizontal configuration, the shock tube produces a normal shock wave. As the inclination increases, oblique shocks are obtained. The entirety of the data gathered in this study was at the horizontal

configuration, therefore the shock wave produced during an experiment is normal to the initial conditions.
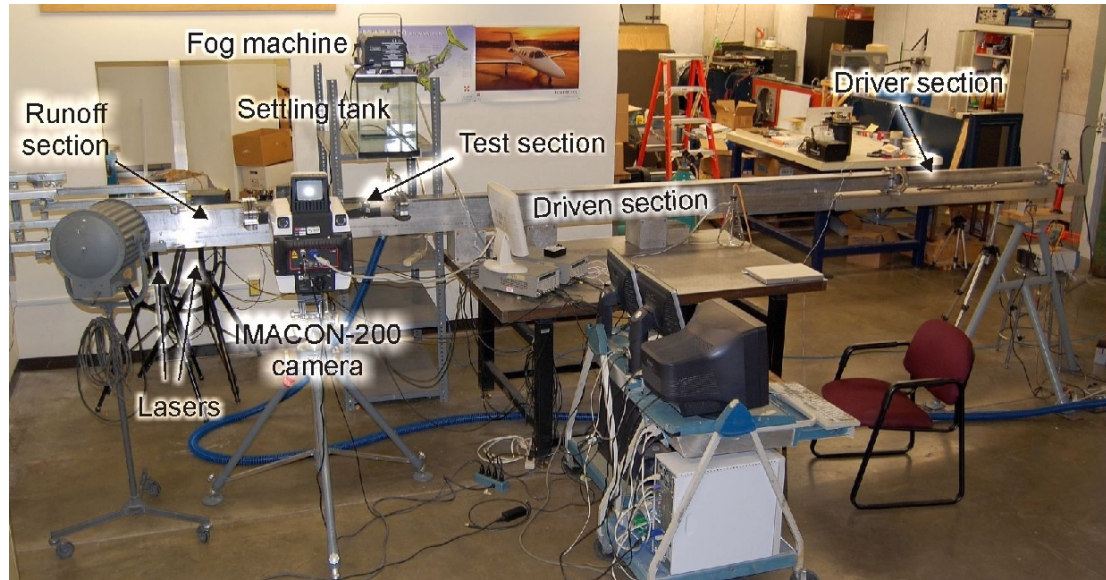
Figure 3.2: Image of UNM Shock Tube [15].

The driver, driven and run-off sections are all manufactured from 6061-T6 aluminum with modular mounting flanges used to attach the sections. The driver section is 1.22m in total length, and is composed of circular 101.6mm outer diameter extruded tube with 12.7mm wall thickness, for an inner diameter of 76.2mm. Its robust design allows for a maximum pressure corresponding to a test experiment at a velocity of Mach 4.0, however the tests conducting in this study were for Mach 1.67 and 2.0. The driver sections circular construction alleviates stress concentrations during pressurization [16]. Typically, the pressurizing gas used during an experiment is Helium, for its abundance and relative inexpense. Separating the driver and driven sections is a polypropylene diaphragm. Diaphragms vary based on the desired Mach number for the experiment, but are typically CG5000 and CG6000 transparencies manufactured by 3M for Ma $= 1.67$ and Ma$=2.0$, respectively. Multiple transparencies

are commonly layered to achieve higher pressures of Helium. Alternatively, paper diaphragms can be used during testing for low Mach numbers, near 1.22 [15].

At the time of an experiment, the test tube operator first must install the required diaphragm(s) between the driver and driven sections. The operator then initiates pressurization of the driver section via an electric solenoid and switch connected to the driver gas bottle, regulated to a pressure of 80psi and 180psi for Ma= 1.67 and Ma = 2.0, respectively. Driver section pressure is monitored with a pressure transducer and digital readout. When the pressure reaches a certain limit, the operator ceases pressurization. Due to the polypropylene construction of the diaphragms, stretching occurs at high pressure. The operator must allow the diaphragms to reach equilibrium, and continue pressurization until the desired limit is met. This manual operation of the pressurization process allows the operator to account for variations in temperature and barometric pressure, as opposed to manufactured burst discs used in other experiments which auto rupture based on stress [30]. Feedback is provided to the operator after an experiment is conducted, based on the velocity of the shock wave, given by diagnostic equipment discussed in a later section.

Once the desired pressure of the driver section is obtained and has stabilized, the operator ruptures the diaphragms with a linearly actuated puncture head. Concentrically mounted inside the driver section is the controlled rupture mechanism. The mechanism consists of a shaft mounted on linear bearings, which moves via a linear electronic solenoid. Near the diaphragm end of the driver section, a puncture head, Figure 3.3, is mounted on the shaft. The puncture head pierces the diaphragms, removing the boundary between the driver and driven section, allowing the pressurized helium to expand downstream and form a normal shock wave. Use of the puncture head creates consistent diaphragm ruptures, shown in the data acquisition section of this chapter.

Figure 3.3: Image of the puncture head used to rupture diaphragms between the driver and driven sections of the shock tube.

The driven section is constructed from 3.2m long, 101.6mm square tubing with 12.7mm wall thickness for a 76.2mm (3inch) square inner dimension. Although the pressurized gas (and shock wave) escaping the driver section must transition from a round to square cross section, the length of the driven section allows the flow to normalize and form a planar normal shock wave. Atop the driven section are two Omega pressure transducers separated at a distance of 2.59m. The pressure transducers relay information to the operators control console for data logging, and transmit a signal used for image collection. Following the flow downstream, the next section attached to the driven section is the test section. For brevity sake, details of the test sections used in this study are elaborated on in more detail in Section 3.2. Immediately following the test section is the runoff section, constructed of 6061-T6 aluminum with same dimensions as the driven section, less overall length. The length of the runoff section is 0.61m, and was designed to limit any interference from reflected shock.

3.2 Test Sections

Transparent polycarbonate test sections are used to visualize the initial conditions within the shock tube. The initial conditions vary from each study conducted at the UNM shock tube facility. With varying initial conditions, the test sections are often varied accordingly. This particular thesis studies the differences in boundary layer growth behind the normal shock for two test sections. The subsections below elaborate on the uses for each test section, and how the test section geometries differ.

3.2.1 Injection Test Section

As mentioned in Section 2.3, the University of New Mexico has a long lineage of studies conducted to better understand Richtmyer-Meshkov Instability (RMI). Particularly, the works of Anderson [15], White [16], and Olmstead et al. [17] focus on RMI growth and transition to turbulence of a cylindrical gas column. In their experiments, Sulfur Hexafluoride(SF_6) is bubbled through acetone in a graduated cylinder, causing the SF_6 to evaporate and transport minute acetone droplets to a 75L settling tank above the test section. The multiphase initial conditions were injected into the test section as a cylindrical column via a 6.35mm stainless steel tube within a 15.875mm plastic tube. The concentric tube arrangement allows a co-flow of air around the column of SF_6 and acetone, preserving the laminar state of the column. The velocity of the seeded gas column and co-flow of air is roughly 10cm/s [15], 3 orders of magnitude less than the velocity of the shock wave experienced during the test.
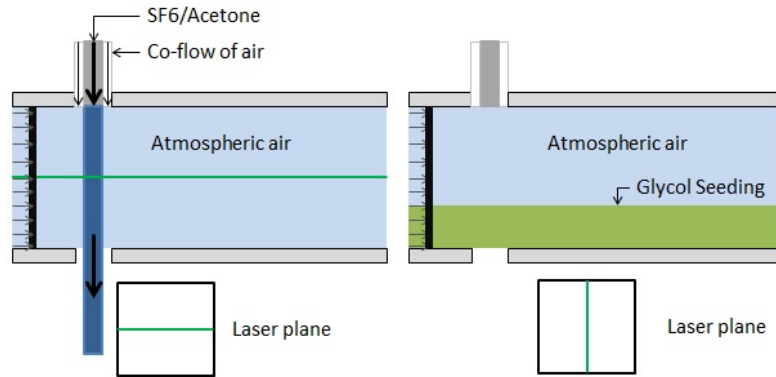
Chapter 3. Experiment Setup

Figure 3.4: Schematic of the test section used by Anderson [15], White [16], and Olmstead et al. [17], on the left, and a schematic of the test section used for the studies in this thesis on the right.

During their tests, the seeded gas and co-flow of air must remain perfectly cylindrical before the shock wave imposes its pressure gradient on the initial conditions. To meet this requirement, the initial conditions flow from the settling tank above the test section, through a hole in the top of the test section, through the internal cross section, and out through the bottom of the test section. This is achieved by drilling two 15.875mm holes through the top and bottom of the test section. Discussed in Sections 2.3 and 2.4, the boundary layer growth of the accelerated gas column appears much larger than the anticipated values from Mirels [18, 25]. This thesis evaluates the boundary layer growth specifically by utilizing particle image velocimetry (PIV) to visualize the flow at the lower boundary of the test section for flows of Mach number 1.67 and 2.0. To directly measure the boundary layer growth seen in Anderson [15], White [16], and Olmstead et al. [17], the same polycarbonate test section with the injection holes for the gas column is evaluated.

3.2.2 Baseline Test Section

The boundary layer growth phenomena witnessed in the work of Anderson [15], White [16], and Olmstead et al. [17] is believed to be caused by the injection holes from the seeded cylindrical gas column. As a baseline, a geometrically similar test section is also used during this study to evaluate the boundary layer growth behind a shock, with one distinguishing difference. The second test section used in this series of experiments, see Fig 3.5, does not have the injection holes drilled through the test section. By installing a test section without the holes, the flow has no source of redirection.
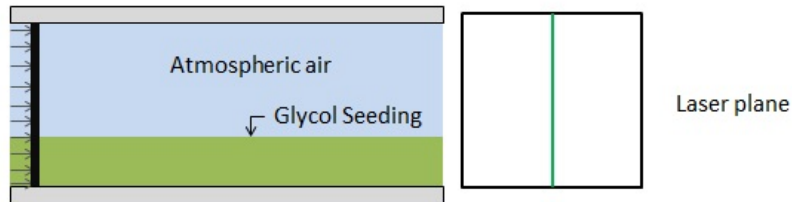
Figure 3.5: Schematic of the baseline test section used for the studies in this thesis.

3.3 Particle Seeding

To visualize the behavior of the accelerated flow after shock passage, the quiescent air is seeded with liquid glycol droplets acting as tracer particles. The size of the glycol droplets vary between 0.5-3μm. Comparatively, the glycol droplets are much larger than the acetone droplets used for visualization in the RMI studies, which causes them to significantly lag behind the shock. This lag is documented in Chapter 4, as is the volume fraction of the glycol particles.

Seeding is attained by a recreational fog (smoke) machine. Liquid glycol is

deposited in the fog machine's internal reservoir. Operation of the device is managed with a momentary switch, which injects the liquid glycol onto a heating element within the machine. The glycol vaporizes, and leaves the machine as a fog, common for holiday theatrics and disc jockeys.

Heating the glycol causes two issues. One, directly mixing the stationary air with the heated glycol affects the state characteristics of the air, which is detrimental to the experiment. Two, the heated droplets tend to be less dense than air. The buoyancy of the heated glycol vapor causes the glycol to rise, also detrimental to the experiment. The data acquisition and imaging is setup to gather an image close to the lower boundary of the test section. Heated glycol rises out of the frame of the image, resulting in zero exposure of the flow field within the test section. The glycol vapor must be cooled before mixing with the air in the test section to mitigate the buoyancy effects.
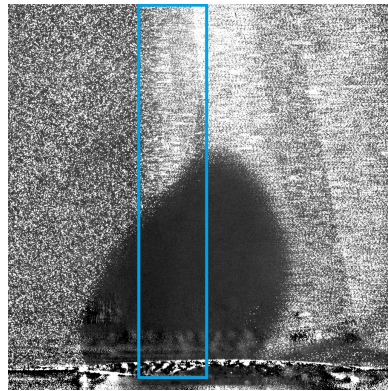
Figure 3.6: Heated glycol droplets are suspended in the test section and accelerated as the shock wave travels downstream. Chilled glycol droplets fall out of suspension when exposed to cooler atmospheric conditions underneath the injection hole, resulting in a void of glycol seeds for visualization of the flow. The region of the passing shock wave is outlined in blue.

Cooling and mixing of the glycol occurs in a 75-liter settling tank above the

test section. Heated glycol vapor leaves the fog machine and is deposited into the settling tank. The glycol stream is directed into a vessel filled with ice. The ice cools the glycol, while a miniature computer fan fed by a 12V power source mixes the chilled glycol with air inside the settling tank. Once the glycol is fully mixed and chilled, it is plumbed through the downstream end of the runoff section, into the test section, and deposited.

It is worth noting the glycol seeding process is not straight forward. As heating caused issue with the glycol vapor rising, cooling causes a similar issue. Cooling the glycol too much allows the glycol to condense beyond the vapor state, and become a liquid within the test section. The liquid glycol clings to the sides of the transparent polycarbonate test section and clouds the visibility of the camera through the test section walls. The clouding effect can render experiments ineffectual if the test section is not cleansed of deposited glycol.

There is also a key balance between too much and too little glycol seeding. The DaVis software used to analyze the images prefers heavy, dense seeding of the glycol for best visualization results of the particle image velocimetry (PIV), which is discussed in greater length in Chapter 4. However, dense seeding leads to four-way coupling, as discussed in Chapter 1 [13]. This four-way coupling has an negative effect on the accelerated flow within the test section, causing the particles to unnaturally alter the turbulent behavior of the boundary layer. Glycol seeding requires a keen eye and steady hand for striking a balance between too much and too little, for optimal flow visualization results.

3.4 Data Acquisition

Data acquisition for the UNM shock tube facility is separated into three sections: shock wave velocity measurement, test section illumination, and test section imaging.

Velocity measurement occurs in the driven section, when the normal shock wave passes over two Omega pressure transducers. The pressure transducers relay data via a National Instruments PXI-1002 board with a digital oscilloscope, and ultimately to a computer for storage. A sample of the stored data is shown in Figure 3.7, a readout of pressure vs. time. Post processing and analysis is performed on each of these sample data records to obtain the shock velocity. The pressure transducers are mounted atop the driven section and separated by a distance of 2.59m. Dividing this distance by the time between the rise in pressure from the upstream and downstream transducers yields the average velocity of the shock.
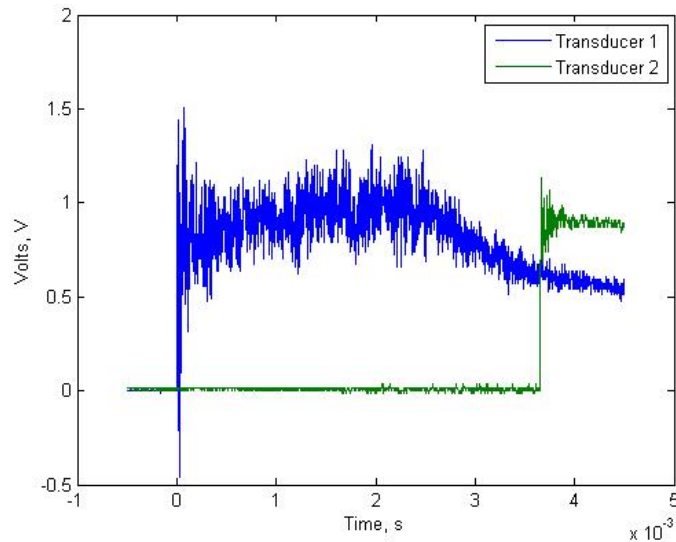

Figure 3.7: Example of data readout from pressure transducers 1 and 2. Pressure rise in each transducer indicates shock passage. Time between pressure rise of transducers 1 and 2 is used to verify shock velocity.

The downstream pressure transducer also serves the function of initiating the illumination of the test section. The signal from transducer 2 is fed into two Stanford Research DG-535 digital delay generators. The delay generators delay the trigger signal by a value set by the operator, and forwards the signal to the illumination system. Illumination of the test section is provided by two New Wave Gemini double-pulsed Nd:YAG lasers. Each laser pulse is triggered by an individual signal from one of the two DG-535 delay generators [15].

Two double-pulsed Nd:YAG lasers allows for 4 exposure sequences per experiment, each with a duration of 5ns. Laser pulses are emitted 500ns apart at 532nm with an optical energy of roughly 0.2J per pulse. Lasers are mounted on a tripod aside the shock tube with a cylindrical and a spherical lens, which expand the laser beam into a sheet. For the study presented in this thesis, the sheet is directed downward through a mirror and held vertical with respect to the horizontal test section.

Figure 3.8: Apogee Alta U42 Camera used to gather images during experiments.

Imaging of the illuminated test section is provided by an Alta U42, an Apogee high performance 4-megapixel cooled CCD camera, which is ideal for exposure at 532nm due to its mid-band coating having the highest peak in the visible wavelength range [16]. Camera position adjustment comes from a tripod mount alongside the

test section, and the camera is mounted upright to capture the horizontal flow within the test section, shown in Figure 3.8. The camera is positioned at the lower level of the test section to capture the lower 2cm of the flow field. This area of focus produces the best resolution of the boundary layer growth behind the shock. The camera is capable of moving further downstream, but for the extend of this study, the camera remains in the same postion to capture the velocity field and vorticity of the flow at the injector site. Previous experiments in the UNM shock tube facility by Anderson [15], White [16], and Olmstead et al. [17] have reversed the positioning of the camera and lasers to capture the horizontal rather than the vertical plane, but the focus of this study will be on the vertical plane.
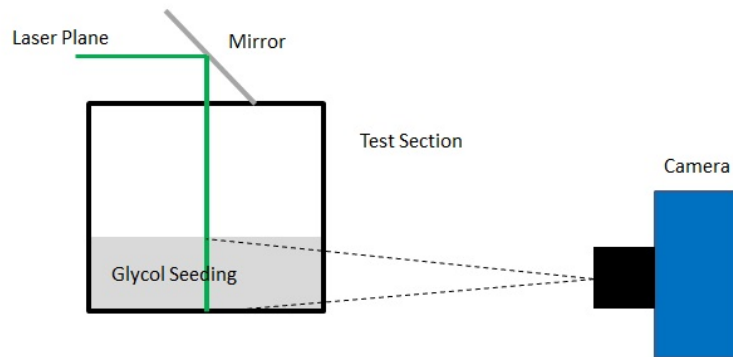
Figure 3.9: Schematic of Camera Positioning relative to test section. The camera is perpendicular to the test section, and focused at the lower boundary of the accelerated flow.

Image capture for an experiment consists of two images; one background image before the propylene glycol/air mixture is deposited in the test section, and one image of the flow field. The illumination of the flow field images varies from time of shock passage to 400μs after shock. Details of the image processing are given in Chapter 4.

Chapter 4

Image Processing

The need to measure fluid flows has followed scientists, researchers, and engineers alike, due to the widespread use of fluid dynamics in a variety of disciplines. While computerized simulations have drastically decreased research time and effort, experimentation continues to be a necessity for validating computer models. This chapter will focus on explaining laser velocimetry, the specific PIV analysis software used in this study, and the processing of each image for data collection.

4.1   Pulsed Laser Velocimetry

Fluid flows vary in size and complexity, ranging from convective flows of air or gas, to laminar flows over aircraft wings, to highly developed turbulent flows in mixing devices. Each type of flow has its own optimal imaging technique, including but not limited to thermal anemometers, volumetric flow measurements through orifice meters and Venturi tubes, direct injection flow visualization, optical systems such as Shadowgraph and Schlieren, and laser velocimetry [33].

The concept of laser velocimetry was first discovered by Cummins et al. [34] while measuring the motion of particles suspended in an aqueous solution. During the course of their experiments, they noticed the random movement of particles through diffusion. While measureing the broadening of the laser light spectrum due to the random particle motion, they observed a shift in the light frequency. The shift in frequency was due to convective currents causing particle motion [34]. The concept of measuring particle motion by light scattering came to be known as laser-Doppler velocimetry (LDV).

The basic phenomenon of laser-Doppler velocimetry is the Doppler shift in light from seeded particles in the flow [33]. The shift in the frequency of the particles can be measured, and directly correlated to a change in distance, time, or both with correct scaling. LDV eventually gave rise to pulsed laser velocimetry (PLV), which is similar yet different to LDV. While LDV uses a Doppler shift to measure the frequency of the light scattering in an image field to infer distance between particles, PLV takes a direct measurement of the location of light peaks created during the illumination of tracer particles [35]. The distance between the peaks is the distance between particles. PLV takes many forms, including laser speckle velocimetry, particle image velocimetry (PIV), particle image displacement velocimetry (PIDV), pulsed laser velocimetry, and particle tracking velocimetry (PTV) [33]. Depending on the light source, most PLVs measure 2D flow fields, although 3D flow fields are possible using approaches such as nuclear magnetic resonance [36]. All PLVs follow the same basic setup; marker particles (1-20μm) are deposited in a flow, illuminated with a light source over a finite time, and captured using still-frame or video photography. The distance of each particle movement is determined by measuring the distance between peaks in the light scattering over a finite time, correlating to a velocity measurement. From these measurements, fundamental fluid-dynamic quantities such as vorticity, deformation tensor, and the pressure field can be obtained.

Each of the specific types of PLVs mentioned in the previous paragraph are suited for particular types of flow measurements. Their differences arise from slight alterations in their measurement setups, or in their image processing. A PLV utilizes a pulsed light source for illumination. Typical for 2D measurements, a light source is directed into a thin sheet. The light source varies with each PLV, but common examples are flash lamps or strobes, argon lasers, pulsed ruby lasers, or Nd:YAG lasers. Ideally, lasers are used for their high timing accuracy ($\sim$10ns) and finite timing capabilities ($\pm$ 1μm)[33]. During the illumination, image(s) of the fluid flow are captured with the embedded marker particles. The light illuminates the markers, making them visible, for an instant, then illuminates the flow again. The first light pulse captures the original position of the particles, while the second captures the particles in a different region. Through data processing, the particle displacement can be measured.

The concentration of the marker particles has a large impact on the quality of data gathered from PLV experiments. Low particle seeding (low concentration) causes large distances between particles, with little overlap. This is beneficial for data processing, since there is little overlap in the scattered light from one particle to another nearby. High particle seeding (high concentration) can cause frequent overlapping of the scattered light, causing noise in the data which may be difficult to interpret. In the extreme case, very high particle seeding can cause 'speckle', where the data processing software cannot discern one particle from another, resulting in a useless image [33].

Data processing relies on the probability of light peaks within an interrogation area (or window)[35]. The image(s) gathered from the experiments are broken into smaller areas (typically 128x128 pixels or smaller) for processing. A Fourier transform is performed on the image squares. This transform breaks the individual interrogation

area into a pattern of light/dark Young's Fringes [33]. Particle locations are shown as bright areas, resulting in a peak in the light pattern. The distance between peaks is measured, and thus the distance between particles is obtained.

The data extracted depends on the probability of matching light peaks within an interrogation window. With low density particle seeding, there is a smaller probability of two particles [33] (or the same particle illuminated twice) being in the same interrogation window, depending on the size of the window and time step between light pulses. The smaller probability causes a higher incidence of bad data vectors from the processing software. Higher density seeding has the opposite effect; higher probability of multiple particles in an interrogation window, and better resulting data vectors [33]. Higher density seeding does involve a more complex image analysis. For the best results, the interrogation window size must be adjusted accordingly.

PIV requires two (or more) illumination periods over a finite time to gather locations of particles. However, these multiple periods can be over multiple images. Auto-correlation PIV uses one image exposure, with multiple illumination sequences taken over a long exposure time. The result is an image with particle 'trains', where the particles seem to follow each other. This sequence is one particle traveling over time. The benefit of auto-correlation lies in the equipment used; a single-exposure camera is readily available, and can have high image resolution. The alternative to auto-correlation is cross-correlation where multiple images are taken, each with one illumination period, and the images are processed in sequence. The benefit of cross-correlation is the ability to track particles (PTV) over a sequence of images, thus removing any ambiguity of the direction of the particle motion [35].

4.2 Vector Field Processing

This section will focus on the image processing used in this thesis, and how the vector field was obtained from raw images.

4.2.1 Image Preprocessing

During the individual experiments (or shots) conducted in this study, two images are gathered per experiment. The first image is a background image of the empty test section, void of any glycol tracer droplets. The second image is the image gathered of the tracer particles embedded in the flow. The purpose of this is to eliminate any possible sources of noise in the PIV interrogation. Although there are no droplets to cause light scattering, other features of the test section cause light scattering or 'noise'. Notably, test sections used in the study in this thesis were constructed of 4 pieces of clear polycarbonate. The floor and sidewalls were cut to dimension, and glued together. The rough edge of the cuts, and the bubbles encased in the glue create features which are illuminated by the laser, and create a false peak during the PIV interrogation. Figure 4.1 also shows light reflection around the injection hole in the injection test section.

Figure 4.1: Sample image of the empty test section before an experiment. Notice the light coming from the bottom of the test section at the injection hole, and the seam between the side and bottom.

Each image background is subtracted from the experimental image to remove any light scattering emitted from anything other than the tracer particles. A comparison of an image before and after background subtraction is shown below in figure 4.2.
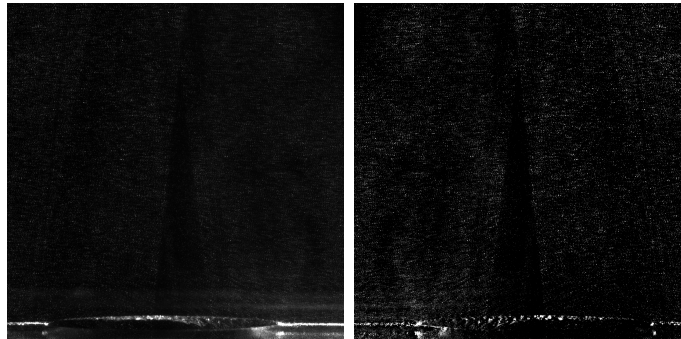

Figure 4.2: The image on the left shows an unmodified experimental image. The image on the right shows the same image, with the background subtracted. Notice the lack of light saturation at the bottom of the subtracted image

Before an image can be processed for PIV, the image orientation must be modified to achieve the desired flow direction. Images gathered from the Apogee Alta U42 arrive with the flow moving from bottom to top. Each image must be

rotated 90° and mirrored about the vertical axis so that the flow direction is from left to right, shown in Figure 4.3.
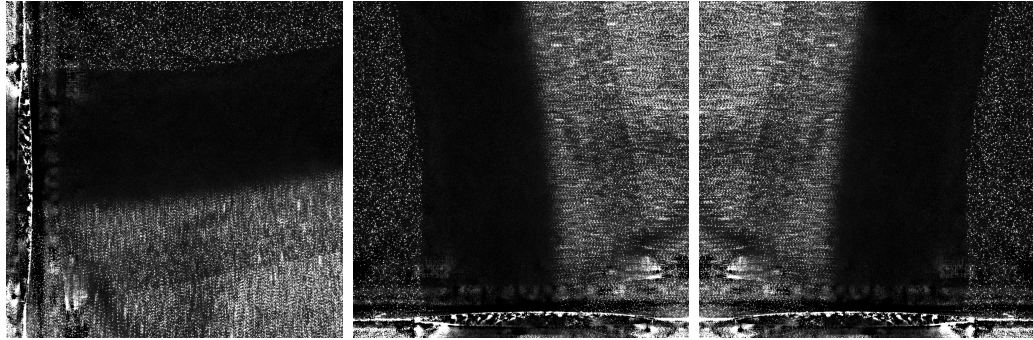

Figure 4.3: The image on the left shows an unmodified experimental image. The image in the middle shows the rotated image, and on the right is the final rotated and mirrored image.

4.2.2 PIV Interrogation

All PIV interrogation used in this thesis was done so with LaVision DaVis Flow-master software [37]. Each image was processed as a 'double frame' image using auto-correlation. Although the image contains multiple light exposures (3-4), the double-frame processing technique was needed for auto-correlation. The effect of using more light exposures per image with the double-frame technique has yet to be determined.

Each image was processed using a multi-pass interrogation, starting with an estimated shift of 8 pixels. Based on the scaling of the image window, and the velocity of the flow, 8 pixels was the average anticipated particle shift. Defining an initial direction with PIV sets a guideline for the interrogation software to follow when establishing fluid flow patterns. Without the initial pixel shift definition, the direction of fluid flow would not be discernible.

Chapter 4. Image Processing

Initial processing passes began with 96 pixel oval windows with 2x greater length than height, since the flow direction is horizontal. Defining a window with these dimensions increases the probability of multiple particles per window, resulting in better data. Each pass ran 50% overlap with decreasing window size, concluding with 32 pixel oval windows. Between each pass, a median filter is implemented. The median filter was setup to remove vectors if the vectors difference to the average vector was greater than 2 times the root mean square of its neighboring vectors. Also, the median filter will re-insert vectors if the difference to average is less than 3 times the root mean square of the neighbors.

Post-processing of vector fields is critical to data clarity. Post processing has multiple steps, beginning with an allowable vector range. Since the velocity of the accelerated flow and the image scale is known, the approximate pixel shift is known for a flow field. The allowable vector range of 12 ± 12 pixels was set in the V_x direction, and 0 ± 7 pixels in the V_y direction. Uneven particle seeding in images was common in this study, resulting in vector fields with empty voids. An interpolation feature in DaVis allowed to fill all voids based on the neighboring vectors. After interpolation, a 3x3 smoothing algorithm was implemented, followed by the allowable vector range again.
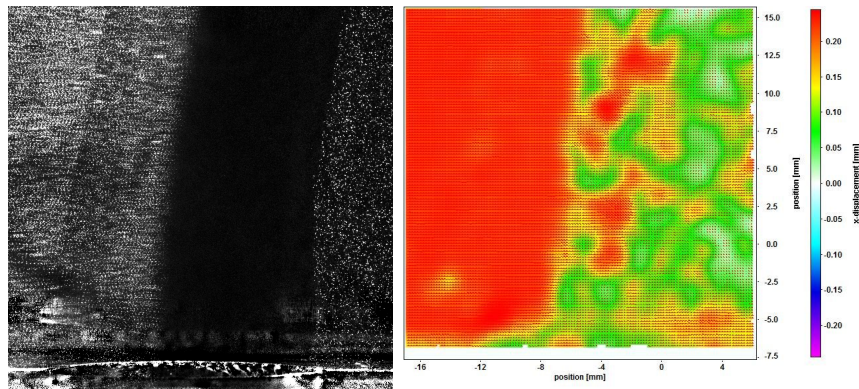
Figure 4.4: The image on the left shows an experimental image before PIV interrogation. The image on the right is the vector field produced by DaVis

Figure 4.4 shows an experimental image of the shock wave passing over the injection hole at Mach 2.0. Flow direction is from left to right. Although the tracer particles are stationary on the right side of the hole, the DaVis auto-correlation finds the stationary particles and interrogates them to believe there is motion.
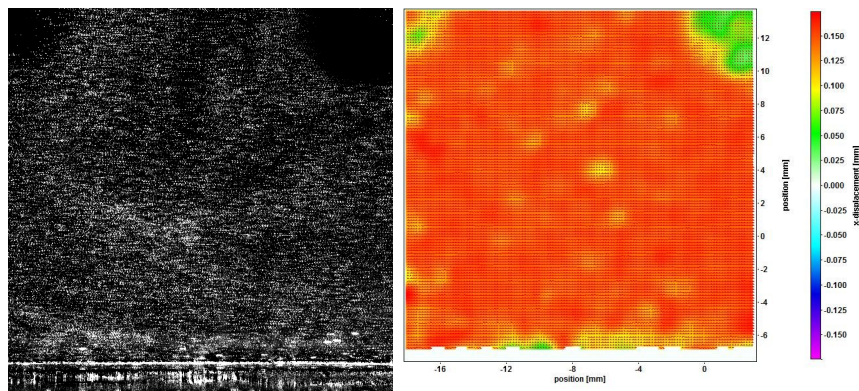

Figure 4.5: The image on the left shows an experimental image with a void of tracer particles in the upper corners. The image on the right is the vector field produced by DaVis. Note the green 'low velocity' areas in the vector field

Figure 4.5 shows the effects of poor particle seeding. Tracer particles must

be evenly dispersed to obtain a quality vector field. If voids exists, a 'fill-all' and smoothing post processing are imposed; the PIV software will attempt to fill and smooth the void, though with poor consequences. The large green areas in the vector field show where no particles existed in the image, and were smoothed through post processing. Similar behavior can be seen due to 'streaking' in the mirror. 'Streaking' is when a feature exists on the mirror, which prohibits the reflection of the laser sheet into the test section. Commonly, the overuse of a laser will burn a hole through the mirror, which needs frequent replacing. The result of this is an illumination sheet with voids, which do not illuminate particles in the empty light area, as shown in Figure 4.6. However, smoothing has added benefit, as shown below in Figure 4.7.
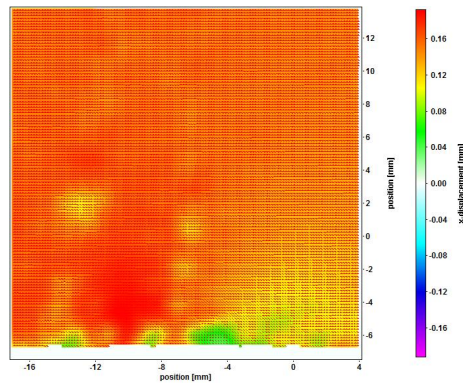

Figure 4.6: The vertical streaks present in the center of the image are artifacts of the mirror not reflecting the laser sheet into the test section completely.
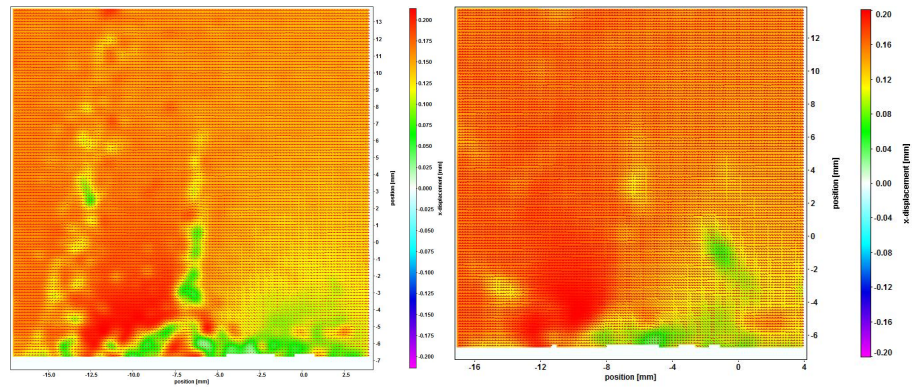
Figure 4.7: The image on the left shows a vector field before the smoothing operation. The image on the right is after the smoothing process. Voids/streaks created by the laser are visibly reduced to remove outliers from the flow field.

Chapter 5

Results

This chapter will present the results from experiments conducted at Mach 1.67 and Mach 2.0 for two test sections, one with an injection hole present, and one without the injection hole, referred to as the baseline test section. A study of the effects of the injection hole test section on the velocity components of the flow, the boundary layer profile, boundary layer growth, and vorticity was performed. From this study, a better understanding of the boundary layer growth within each test section was gathered.

Chapter 5 is separated into 4 areas. First, the velocity in the streamwise direction is analyzed for Mach 1.67 and Mach 2.0 with each test section, for varying experimental times starting with time of shock passage over the injection site, and progressing to 300μs after shock passage. Second, the velocity in the spanwise direction was measured starting with 100μs after shock passage, and continuing to 300μs after shock passage. Third, vorticity for each combination of Mach number and test section was measured for timing 100μs after shock passage, and continuing to 300μs after shock passage. Fourth and finally, a boundary layer analysis for the test sections was conducted to explicitly measure the boundary layer growth in each test section

for varying timings and Mach Numbers. All images in this chapter show the flow direction from left to right.

5.1 Streamwise Velocity

Velocity measurements in the streamwise direction are evaluated in this section. The streamwise direction follows the flow downstream through the test section, and is given as the 'x' direction in the images depicted in this chapter. The purpose of the streamwise velocity measurements is to define the boundary layer height. As mentioned in Chapters 1 and 2, the boundary layer height is the height of the viscous sublayer of fluid flow near the fluid-solid boundary, and is defined as 99% of the free stream velocity in the inviscid layer above.

5.1.1 Mach 1.67

Figure 5.1 captures the shock passage over the injection site for Mach 1.67. On the left is the test section with the injection hole, on the right is the baseline test section. Both images clearly show the shock front, and the region of accelerated tracer particles behind (left) of the shock front. An even distribution of accelerated flow behind the shock is depicted in red-orange, while slower regions are shown in green. It is worth noting that although the green regions are shown as having a velocity profile, they are not moving. Previously mentioned in Chapter 4, the auto-correlation function used for PIV interrogation cannot easily discern a field of stationary particles vs. a field of slow moving particles. The interrogation software then attempts to find patterns within the suspended tracer particles, and assign a velocity value to them. This assignment is false, as it is not from a single particle at one time vs. another,

but rather a pair of particles at the same time.

Although Figure 5.1 clearly shows the shock front for each test section, it is not a beneficial image for the purpose of evaluating differences between the test sections. A planar shock front is clearly shown in each image, but the lower field of the image is clouded with noise. This noise makes definition of the boundary layer difficult. However, for such an early timing it is expected that the boundary layer is zero at time of shock passage, and grows with distance (and time) from the shock front. The lack of definition of the shock profile at the lower boundary in both images is worth noting.
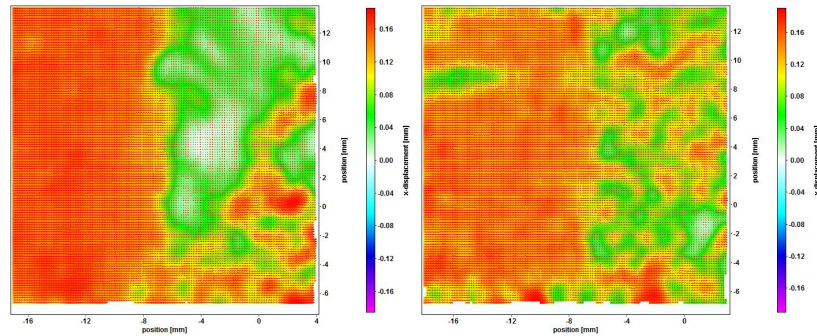

Figure 5.1: Both images show the streamwise component of accelerated flow at time of shock passage over the injection hole for Mach 1.67. On the left is the test section with the injection hole, on the right is the baseline test section. The shock wave is located at x = -7mm in both images. Higher displacement (subsequently, velocity) areas are denoted in red-orange, with lower velocities in yellow-green, shown on the scale on the right.

As distance from the shock front increases with time of shock passage, more interesting behavior can be discerned from each test section. In Figure 5.2, each image shows definitive characteristics. On the left image (with the injection hole), the flow enters the field of view at an expected high velocity, denoted in red. As the flow passes over the injection hole (situated on the floor between -12mm and +3mm), the

streamwise velocity component slows, shown in green. This behavior is not limited to the floor, and grows in the spanwise direction over the injection hole.

On the right image in Figure 5.2, the baseline test section does not share the same behavior with its injection test section counterpart. The flow is shown to have an even distribution at high velocity. In the lower region of the image at the fluid-solid boundary, a definitive area of slowed flow is shown in yellow. This area is assumed to be the boundary layer. The boundary layer of the flow, caused from frictional effects with the wall, has a height of approximately 1mm, which is roughly similar to Mirels' approximation for turbulent flow.
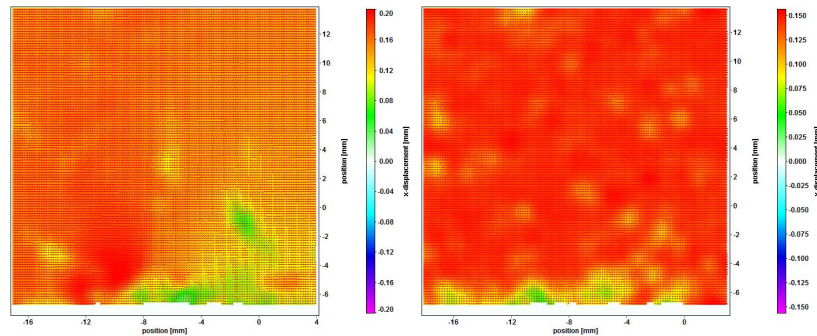

Figure 5.2: The images show the streamwise component of accelerated flow over the injection hole for Mach 1.67. Both images show the flow at time of 100 μs after shock passage over the injection hole. On the left is the test section with the injection hole, on the right is the baseline test section.

Further increasing the time after shock passage yields similar results to Figure 5.3. The streamwise velocity component is shown to stagnate above and downstream of the test section with the injection hole, while the boundary layer in the baseline test section grows in height as Mirels predicted.
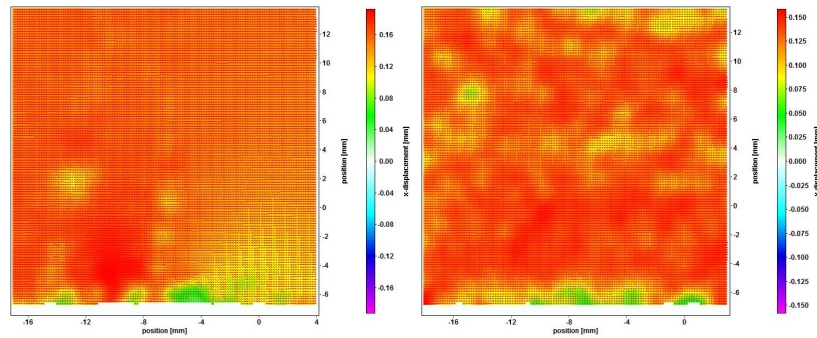
Figure 5.3: The images show the streamwise component of accelerated flow over the injection hole for Mach 1.67. Both images show the flow at time of 200 μs after shock passage over the injection hole. On the left is the test section with the injection hole, on the right is the baseline test section.

By 300μs after shock passage shown in Figure 5.4, the stagnation area downstream of the injection hole is fully defined. Closely examining the velocity above the injection hole (-12mm to roughly +3mm) shows the velocity field has a nearly linear distribution. Below this line (approximately 45° to the horizontal), the flow is stagnated and slowed compared to the upstream velocity. Moving downstream, the stagnation area grows. Above this line, the flow is nearing free stream velocity.
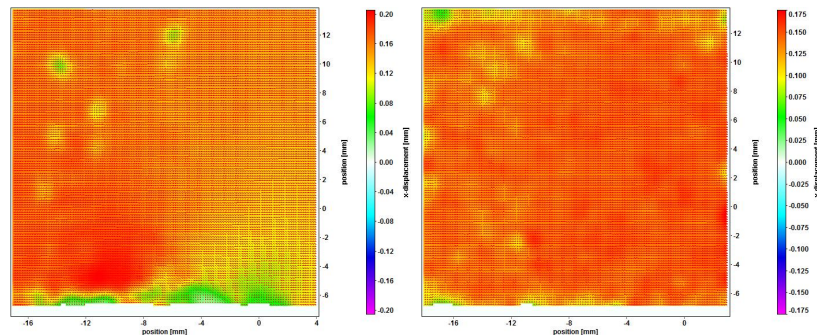

Figure 5.4: The images show the streamwise component of accelerated flow at over the injection hole for Mach 1.67. Both images show the flow at time of 300 μs after shock passage over the injection hole. On the left is the test section with the injection hole, on the right is the baseline test section.

5.1.2   Mach 2.0

Figure 5.5 captures the shock passage over the injection site for Mach 2.0. On the left is the test section with the injection hole, on the right is the baseline test section. In the injection test section, the injection hole is located between -13mm and +2.85mm. Clearly visible in each image is the shock front, similar to Figure 5.1. On the right image, the upper portion of the image with 'slowed' flow should be disregarded. This was a region of uneven particle seeding, which resulted in zero tracer particles in the area. On the left image, the shock front bears resemblance to the planar shock front shown in the Mach 1.67 images. However, the lower region of the shock nearing the fluid-solid interface is more clearly defined in this image. Rather than remaining planar as expected, the image shows two distinct 'steps' in the shock. The lower step occurs at the wall surface near the leading edge of the injection hole, and has a low angle of inclination. At -4mm (centered over the hole), the second step in the shock wave profile is seen, with a high angle of inclination. These steps are not witnessed in the baseline test section.
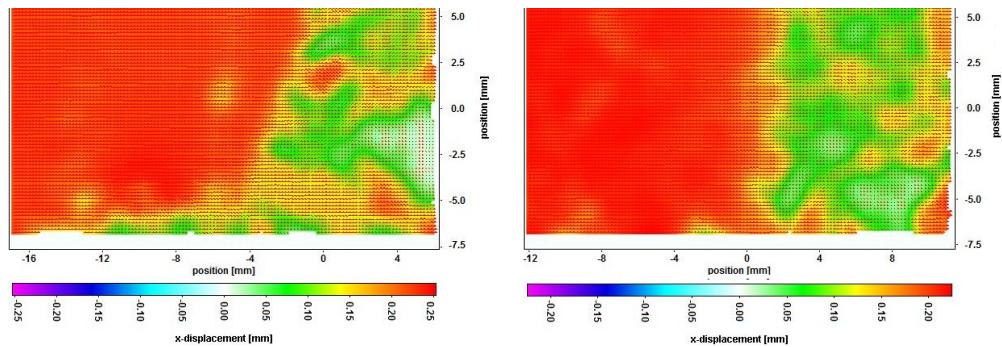

Figure 5.5: The images show the streamwise component of accelerated flow over the injection hole for Mach 2.0. Both images show the flow at time of shock passage over the injection hole. On the left is the test section with the injection hole, on the right is the baseline test section.

Consistent with the behavior witnessed with the Mach 1.67 data, Figure 5.2,

a region of slowed flow starts at the leading edge of the injection hole, and continues downstream as shown in Figure 5.6. This growth appears to be linear, and causes a relatively large region of stagnation after the injection site. On the right image, the baseline test section has no features. It appears the flow field is evenly distributed, with a small boundary layer at the fluid-solid boundary. This image depicts the boundary layer thickness as being ≈0.5mm in height, consistent with Mirels' approximation for turbulent flow at Mach 2.0.

Figure 5.6: The images show the streamwise component of accelerated flow over the injection hole for Mach 2.0 Both images show the flow at time of 100 μs after shock passage over the injection hole. On the left is the test section with the injection hole, on the right is the baseline test section.

Data gathered for Mach 2.0 with the injection test section has proven difficult to analyze. High shock velocities coupled with the difficulties associated with particle seeding has made gathering data at times larger than 300μs difficult. For the few particles that could be processed, (shown in regions of red in Figure 5.7), the flow seems to follow the same stagnation pattern previously mentioned. Prior to the injection site, the high velocity flow reaches nearly to the fluid-solid boundary. After the injection site, the nearest region of free stream flow is located at a spanwise height of 12mm (-7mm to +5mm). For the baseline test section, flow remains constant throughout the test section, with a finite boundary layer of ≈1mm.
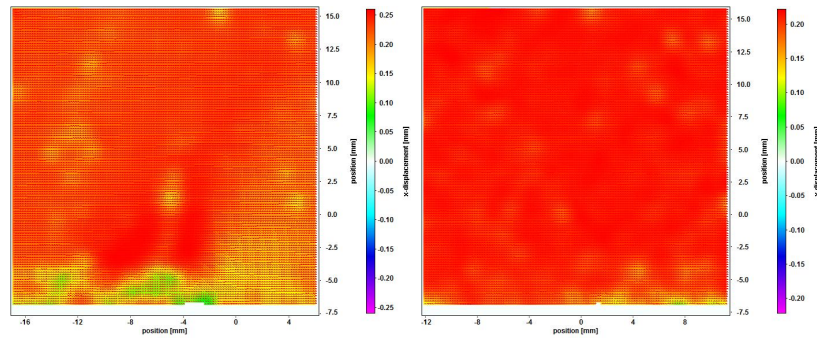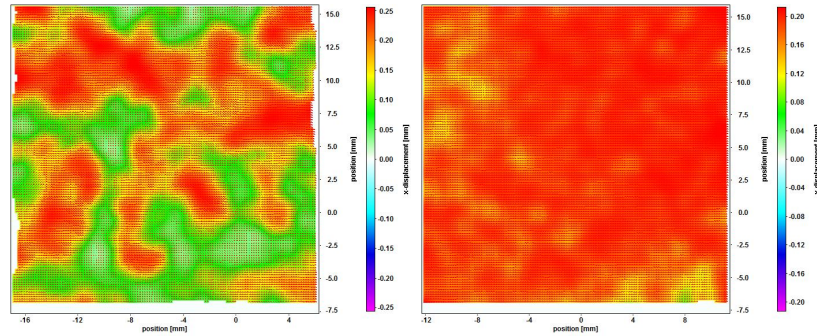
Figure 5.7: The images show the streamwise component of accelerated flow over the injection hole for Mach 2.0. Both images show the flow at time of 300 μs after shock passage over the injection hole. On the left is the test section with the injection hole, on the right is the baseline test section.

5.2 Spanwise Velocity

Velocity measurements in the spanwise direction are evaluated in this section. The spanwise direction is defined as the normal direction to the the flow, or normal to the streamwise direction. The spanwise direction is given on the 'y' axis in the images shown in this chapter. The intention of analyzing data in the of the spanwise direction is to determine if the flow is turning relative to the free stream velocity. Analyses in the spanwise direction were made starting with 100μs after shock passage. Initial measurements were made at time of shock passage, but no discernible data could be recovered from such measurements.

5.2.1   Mach 1.67

Figure 5.8 shows the spanwise velocity component for Mach 1.67 with the injection test section (left) and the baseline test section (right). As expected with the injection test section, a large region of spanwise flow is shown over the injection site. The high energy, pressurized flow within the test section is redirected through the injection hole, and out to lower energy atmospheric conditions. In the baseline test section, no patterns of spanwise flow are seen.
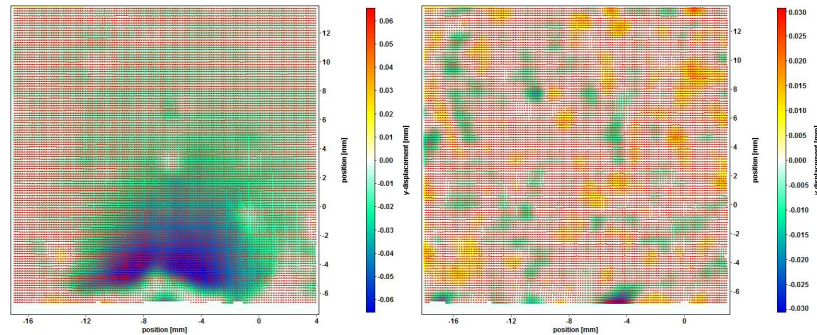

Figure 5.8: The images show the spanwise component of accelerated flow over the injection hole for Mach 1.67. Both images show the flow at time of 100 μs after shock passage over the injection hole. On the left is the test section with the injection hole, on the right is the baseline test section.

Increasing time to 200μs after shock passage as shown in Figure 5.3, shows similar features to timings at 100μs after shock. The region of spanwise flow for 200μs appears to have the same size and magnitude as 100μs after shock. Again, no spanwise flow is shown with the baseline test section.

Figure 5.9: The images show the spanwise component of accelerated flow over the injection hole for Mach 1.67. Both images show the flow at time of 200 μs after shock passage over the injection hole. On the left is the test section with the injection hole, on the right is the baseline test section.

Further increasing time to 300μs in Figure 5.10 shows nearly identical results. The magnitude and location of the spanwise velocity has not varied with time, and the baseline test section has not shown any features of spanwise flow. From the spanwise measurements, it is believed the redirection of the flow from streamwise to spanwise out through the injection hole is the source of the stagnation region downstream of the injection site. As the high energy, accelerated flow encounters an area open to low pressure atmospheric conditions, the flow is redirected through the injection hole. The majority of the flow near the wall is turned in the spanwise direction, resulting in little momentum in the streamwise direction. The lower momentum flow downstream of the injection hole creates a region of stagnation, which was shown in the streamwise measurements in section 5.1.
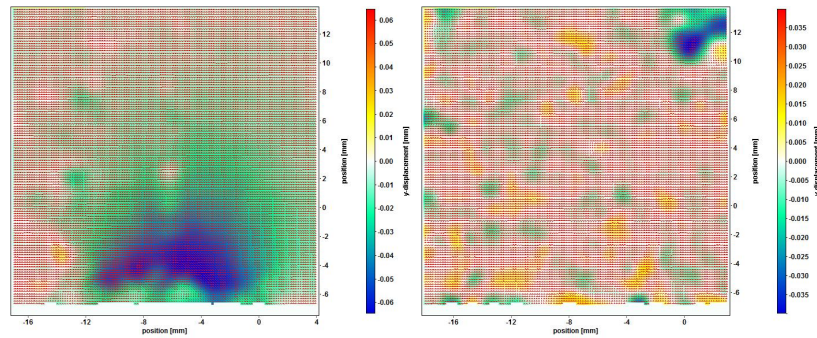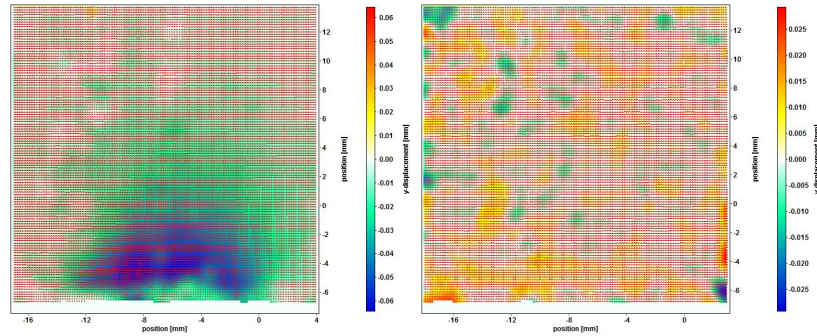
Figure 5.10: The images show the spanwise component of accelerated flow over the injection hole for Mach 1.67. Both images show the flow at time of 300 μs after shock passage over the injection hole. On the left is the test section with the injection hole, on the right is the baseline test section.

5.2.2   Mach 2.0

Continuing the spanwise measurements to Mach 2.0 shows similar results to the analysis shown in Section 5.2.1 with Mach 1.67. A large region of spanwise flow occurs directly above the injection hole site, with no discernible patterns in spanwise flow for the baseline test section. It is worth noting that the size of the spanwise region of flow is smaller for Mach 2.0 than for Mach 1.67. It is speculated this is due to the Mach 2.0 flow having more streamwise momentum than the 1.67 prior to the injection site, resulting in less flow redirected to the spanwise direction and out through the injection site. This, in turn, results in a slightly smaller stagnation area in the streamwise direction for Mach 2.0 (shown in Figure 5.6) than for Mach 1.67 (shown in Figure 5.2).

Figure 5.11: The images show the spanwise component of accelerated flow over the injection hole for Mach 2.0. Both images show the flow at time of 100 μs after shock passage over the injection hole. On the left is the test section with the injection hole, on the right is the baseline test section.
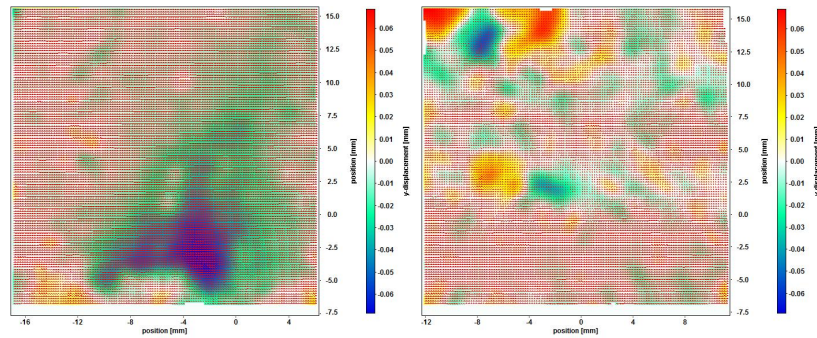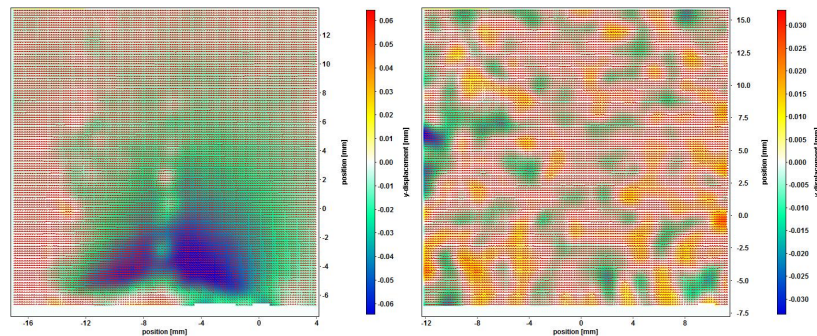

Figure 5.12: The images show the spanwise component of accelerated flow over the injection hole for Mach 2.0. Both images show the flow at time of 300 μs after shock passage over the injection hole. On the left is the test section with the injection hole, on the right is the baseline test section.

5.3 Vorticity

Vorticity is a measure of the turning component of a fluid flow and is obtained by taking a derivative of the velocity vector. Primarily, vorticity is used as an indication of where the redirection of a flow occurs. While it is beneficial, there is inherent error

with vorticity studies since analyses involving derivatives can be quite noisy.

5.3.1   Mach 1.67

Shown in Figure 5.13 below, the vorticity fields of the injection test section (left) and the baseline test section (right) are shown. Previously mentioned in section 5.2, vorticity is expected in the injection test section, since it had a significant amount of spanwise velocity vectors.

Figure 5.13: The images show the vorticity of accelerated flow over the injection hole for Mach 1.67. Both images show the flow at time of 100 μs after shock passage over the injection hole. On the left is the test section with the injection hole, on the right is the baseline test section.

Figure 5.13 indicates there is a turning component of the flow directly above the injection area, but also that the turning component begins shortly before the leading edge of the injection site. The baseline test section on the right shows a random pattern of low vorticity across the vector field, with some turning components located at the fluid-solid boundary.
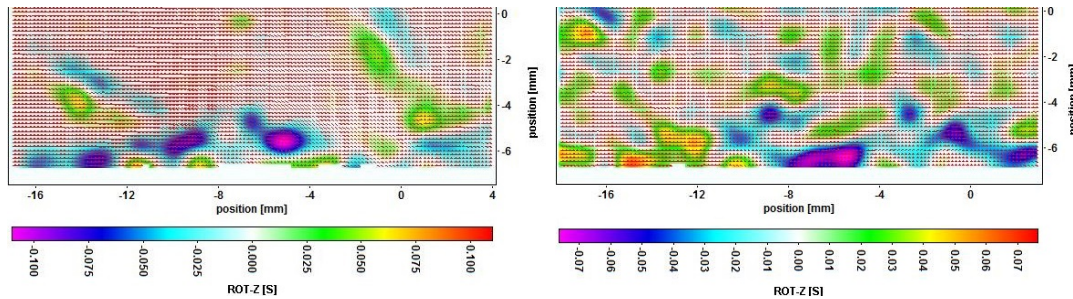
Figure 5.14: The images show the vorticity of accelerated flow over the injection hole for Mach 1.67. Both images show the flow at time of 200 μs after shock passage over the injection hole. On the left is the test section with the injection hole, on the right is the baseline test section.

Increasing the time to 200μs after shock passage shows similar results. Vorticity develops shortly before the leading edge of the injection site (x = -13mm), and continues over the injection site. The magnitude and size of the vorticity is consistent with 100μs after shock, showing no signs of significant growth over time. In the baseline test section, a layer of vorticity is seen at the fluid-solid boundary. It is speculated that this is the viscous sublayer, and that the flow is turbulent due to the random rotational components within the boundary layer.
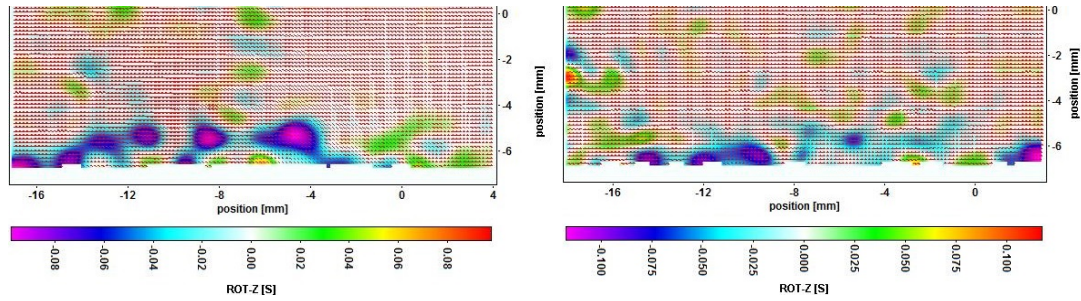

Figure 5.15: The images show the vorticity of accelerated flow over the injection hole for Mach 1.67. Both images show the flow at time of 300 μs after shock passage over the injection hole. On the left is the test section with the injection hole, on the right is the baseline test section.

Figure 5.15 at 300μs shows similar characteristics to earlier timings of Mach 1.67, with no noticeable growth in the vorticity magnitude or region for the injection test section.

5.3.2   Mach 2.0

Continuing the vorticity analysis to Mach 2.0 shows similar yet different behavior to Mach 1.67. The region of vorticity occurs in the same streamwise location as Mach 1.67 (-13mm to -2mm) but extends to a larger spanwise height, as shown in Figure 5.16. The baseline test section follows the same profile as its 1.67 counterparts, with a turbulent boundary layer visible at the fluid-solid interface.
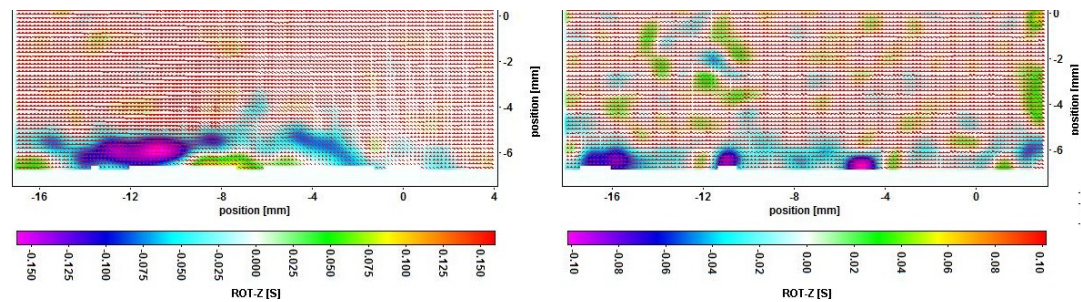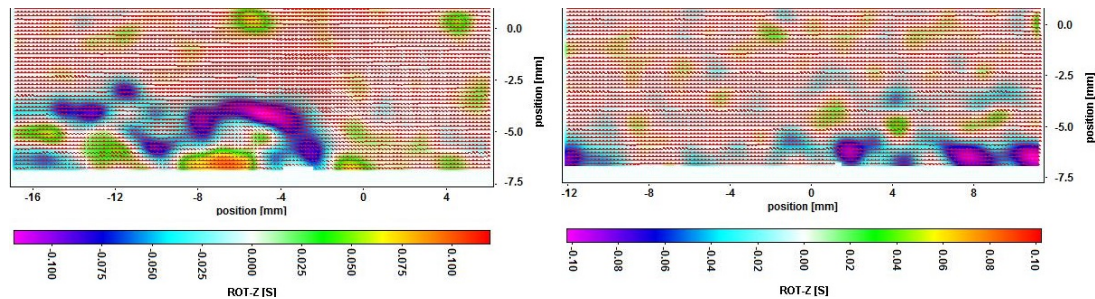

Figure 5.16: The images show the vorticity of accelerated flow over the injection hole for Mach 2.0. Both images show the flow at time of 100 μs after shock passage over the injection hole. On the left is the test section with the injection hole, on the right is the baseline test section.

5.4   Boundary Layer Analysis

To compare the injection section and baseline test section, a study was conducted on the boundary layer velocity profiles for various images over multiple timings and Mach numbers. The study was performed by exporting the streamwise vector fields

of the images from DaVis to MatLab, and using MatLab to average the streamwise velocity vectors based on spanwise height. Each image is broken into a vector field with dimensions 128x128 vectors. The fields were then averaged in the streamwise direction, resulting in an average velocity for a given height, which was then normalized with respect to the maximum average velocity. This data was plotted for each test section and shock velocity vs. time.

5.4.1   Raw Data

The averaged streamwise velocity profiles for Mach 1.67 are shown below in Figure 5.17. On the left is the injection test section data, and the right is the baseline test section data. The data shows a definitive pattern, although with a significant amount of noise. By locating the crossover point where the fluid velocity reaches 99% of the free stream velocity, the boundary layer height is the height of the region whose flow velocity is less than 99%. Figure 5.17 does however, show that the boundary layer is slightly larger for the injection test section compared to the baseline test section. As timing after shock passage is increased (denoted by the multiple curves on each plot, see legend), this boundary layer height is shown to also increase.

Figure 5.17: On the left is the boundary layer profile data for the test section with the injection hole, on the right is the baseline test section. Note that apparent fluctuations in the freestream are due to vectors in poorly seeded areas.

The averaged streamwise velocity profiles for Mach 2.0 are shown in Figure 5.18 below. The injection test section produced much less consistent data for Mach 2.0.
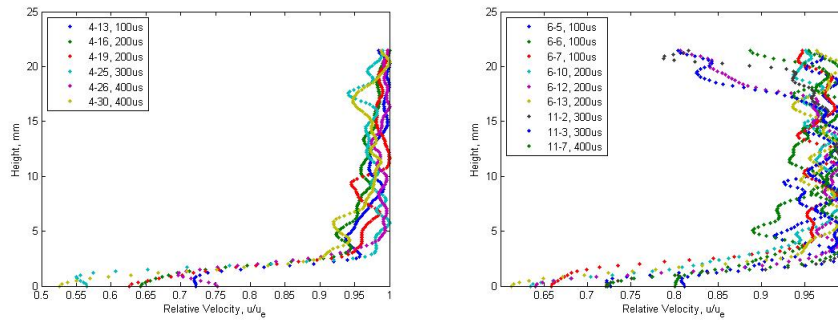

Figure 5.18: On the left is the boundary layer profile data for the test section with the injection hole, on the right is the baseline test section.

5.4.2   Curve Fitting

Due to the noise associated with the raw data, curve fitting was performed on the data for ease of comprehension. The curve fits were performed using a general second

power exponential equation with the form $y = ae^{bx} + ce^{dx}$ with 95% confidence. Figure 5.19 above shows the curve fits for Mach 1.67 at various times after shock passage for the injection test section (left) and baseline test section (right). The boundary layer height for the injection test section is consistently larger than that of the baseline test section. To evaluate the boundary layer height, the slope of the curve fit near the fluid-solid interface must be expanded linearly until it reaches the right boundary, where the velocity relative to the free stream velocity is 1. The height of this intersection point is the height of the boundary layer.
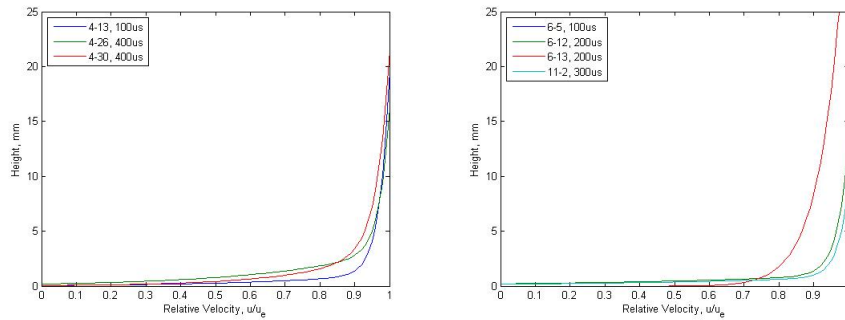
Figure 5.19: On the left is the boundary layer profile curve fit for the test section with the injection hole, on the right is the baseline test section.

Figure 5.20 below shows the curve fit for Mach 2.0 for the injection test section (left) and baseline test section (right). Consistent with the Mach 1.67 data, the injection test section boundary layer height is consistently larger than the baseline test section.
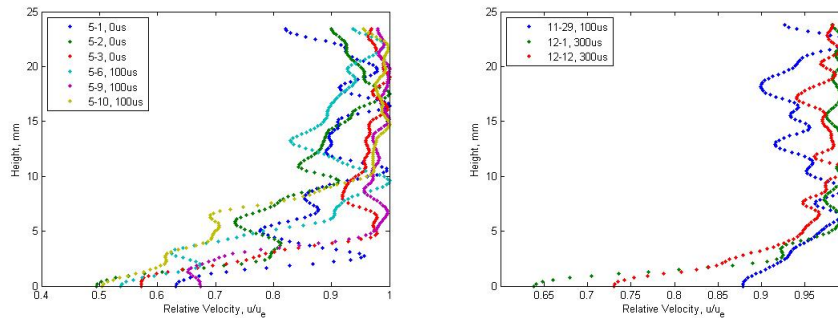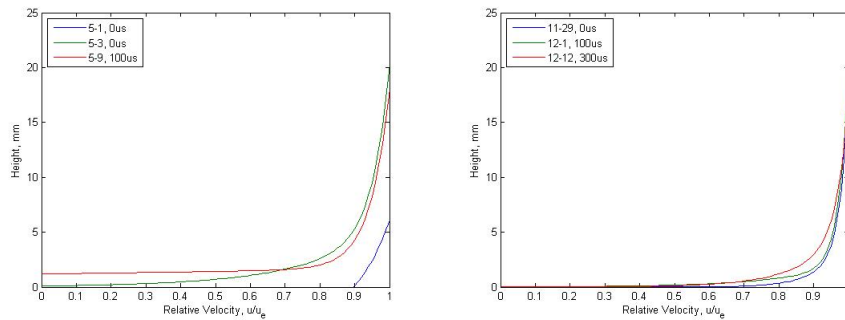

Figure 5.20: On the left is the boundary layer profile curve fit for the test section with the injection hole, on the right is the baseline test section.

It is worth noting that the data from the boundary layer analysis conducted in this section should not be considered exact. The purpose of the study was simply to evaluate trends between the two test sections. The method of averaging the stream-wise vectors for the injection test sections has error associated with it. Specifically,

the stagnation regions shown in Figures 5.2 and 5.6 in Section 5.1 explain the source of the error. The free stream velocity upstream of the injection site extends nearly to the fluid-solid interface. After passing the injection site, there is a linear growth in the streamwise stagnation region. As a result of the method used for the boundary layer analysis, high velocity regions and low velocity regions of flow are averaged at the same spanwise height. Therefore, the boundary layer height is not consistent across the entire field of view.

Chapter 6

Conclusion

This thesis presents experimental results for boundary layer growth generated by impulsive acceleration of a quiescent flow by a normal shock wave in two different test sections, one with an injection hole with diameter 15.875mm and one without the injection hole, at Mach number 1.67 and Mach 2.0. In both cases, stationary air was seeded with glycol droplets used as visualization tracers. All work was performed at the University of New Mexico shock tube facility. The experimental images were obtained by illuminating the seeded flow in the vertical plane in the center of each test section. By varying exposure timing, images were gathered from time of shock passage to 400μs after shock passage for each test section. Images gathered were analyzed using particle image velocimetry (PIV) to obtain flow fields for each data set. Two cases were examined; first, a test section used by Anderson [15], White [16], and Olmstead et al. [17] in their study of Richtmyer-Meshkov instability was analyzed for boundary layer growth in the presence of an injection site at the upper and lower boundaries of the test section. Second, the boundary layer growth of a baseline test section devoid of the injection holes was analyzed. It was found the boundary layer growth of each test section differs drastically.

In the case of the injection test section, analysis of the streamwise velocity component (V_x) showed a large stagnation area immediately after the injection site. The stagnation was found to begin at the lower boundary of the test section near the center of the injection site, and grow linearly in the downstream direction. This type of flow field has previously been recognized by Chyu et al. [14] in the study of shock wave-boundary layer interaction with a bleed slot. In the work by Chyu et al., it was found that weak expansion waves at the leading edge of the bleed hole, and a barrier shock at the downstream edge caused the rapid change in boundary layer height.

Analysis of the streamwise velocity component in the baseline test section showed no distinguishing features of disturbed flow, as expected. The traveling normal shock wave accelerated the air within the test section, and a boundary layer was found to grow behind the shock. The height of the boundary layer, along with the growth rate, closely corresponds to the work performed by Mirels [18, 24, 25, 26, 27] for turbulent boundary layer growth.

Evaluation of the spanwise velocity component yielded similar results for both Mach 1.67 and Mach 2.0. No significant change in spanwise velocity was observed for the baseline test section at either shock velocity. For both shock velocities in the injection test section, a large region of spanwise flow was observed at the lower boundary of the test section, slightly before the injection site and continuing after the injection site. This indicates a large redirection of flow from the streamwise direction upstream of the injection site to the spanwise direction and out through the injection hole. This redirection of flow out of the injection hole results in a stalled region of streamwise flow downstream of the injection site, causing a rapid change in boundary layer height.

Vorticity computations were made for each test section. For the injection test section, vorticity pockets develop at the leading edge of the injection hole, and cease

at the trailing edge. These regions of developed vorticity prove the flow is redirected from the streamwise direction to the spanwise direction, and out through the injection hole. For the case of the baseline test section, vorticity was observed at the fluid-solid interface at the lower wall of the test section. This vorticity was not as consistent in location (streamwise) or magnitude in the injection section. The randomness of the vorticity in location, direction, and magnitude, is attributed to the turbulent boundary layer. The height of the regions of vorticity in the baseline test section correspond to the height of the boundary layer in the streamwise evaluations for similar timings.

Having compared the baseline boundary layer growth to the injection hole test section, it is concluded that the injection site is the primary cause of the rapid boundary layer growth in the injection test section, as compared to a test section with no flow disturbing features. However, the exact reason for the rapid growth has yet to be determined. From evaluation of Olmstead's et al. [17] data from the American Physical Society, Division of Fluid Dynamics Annual Meeting in 2013, it can be ascertained the growth is due to a non-normal shock acceleration of the initial conditions. Olmstead et al. presents an oblique shock interaction with a gas column interface, as shown in Figure 2.7. The observed phenomenon is known as Richtmyer-Meshkov Instability, which is caused by a misalignment of the density and pressure gradients in a shock accelerated flow. The vorticity we see in Figure 2.7 suggests that either the gas column has been rotated to alter the orientation of the density gradient (impossible, since the column remains at a constant location relative to the test section), or the shock is distorted and no longer perfectly planar. In the work of Chyu et al. [14], small expansion waves were shown to exist at the leading edge of the bleed slot, with a barrier shock forming at the trailing edge as seen in Figure 2.3. Near the injection hole, a regular planar shock structure is significantly distorted, as Figure 5.5 confirms.

6.1 Future Work

In addition to the work conducted in this study, the data already collected will be improved by conditional averaging and other post-processing techniques to form the basis for a paper to be submitted to Experiments in Fluids.

To conclusively prove the cause of the rapid boundary layer growth in the test section, the author recommends three new studies be performed. First, the study conducted herein should be repeated using a high-speed multiframe camera in conjunction with the LaVision DaVis image processing software with cross-correlation. The noise introduced from the auto-correlation used in this study resulted in a large amount of unusable data, which was rejected from the study. Cross-correlation would reduce the noise, as well as introduce the capability of particle tracking velocimetry (PTV).

Second, a similar study to the one conducted herein should be pursued for downstream data. The focus of this thesis gathered data at the location of the injection site for the injection test section and at the same downstream distance for the baseline test section. This has enabled this thesis to focus on the effects directly at the injection site, but has limited the study to that region. It is proposed to conduct the same study at various regions downstream of the injection site to quantify the boundary layer growth aft of the injection hole.

Finally, the author recommends Schlieren/shadowgraph imaging be performed at the injection site. Schlieren/shadowgraph images allow for illumination and imaging of density gradients in the flow. To this end, the passing shock wave over the injection site could be imaged. Imaging of the shock wave orientation would allow for broader understanding of the boundary layer growth at and after the injection site.

Appendices

Appendix A

Mirels' Laminar Boundary Layer Approximation

Mirels' approximation [38] starts with the equations of mass, momentum and energy conservation and applies the following boundary conditions:

$$u(x,0) = -\bar{u}_s \tag{A.1}$$

$$v(x,0) = 0 \tag{A.2}$$

$$T(x,0) = T_w \tag{A.3}$$

$$u(x,\infty) = u_e \tag{A.4}$$

$$T(x,\infty) = T_e \tag{A.5}$$

Holding T_w constant, and transforming the mass, momentum and energy conservation equations into a system of ordinary differential equations, from continuity there exists a stream function ψ where

$$\frac{\partial \psi}{\partial y} = \frac{\rho u}{\rho_w} \tag{A.6}$$

Appendix A. Mirels' Laminar Boundary Layer Approximation

$$\frac{-\partial \psi}{\partial x} = \frac{\rho v}{\rho_w} \tag{A.7}$$

A similarity parameter η is defined as

$$\eta = \sqrt{\frac{1}{2} \frac{u_e}{x\nu_w}} \int_0^y \frac{T_w}{T} dy \tag{A.8}$$

and the stream function becomes

$$\psi = \sqrt{2u_e x\nu_w} f(n) \tag{A.9}$$

Note, that $f' = \dfrac{u}{u_e}$. Assuming viscosity varies linearly with temperature,

$$\mu = \left(\frac{\mu_w}{T_w}\right) T \tag{A.10}$$

and applying to momentum yields the Blasius Differential Equation

$$f''' + ff'' = 0 \tag{A.11}$$

Applying the following boundary conditions:

$$f(0) = 0 \tag{A.12}$$

$$f'(0) = \frac{u_w}{u_e} \tag{A.13}$$

$$f'(\infty) = 1 \tag{A.14}$$

Assuming the Prandtl number σ is constant, and temperature as a function of η, the energy equation becomes:

$$T'' + \sigma f T' = -\sigma(\gamma - 1)M^2(f'')^2 \tag{A.15}$$

The general solution for T can be expressed as the linear superposition for adiabatic conditions plus the effects of heat transfer; $\dfrac{T}{T_e}$ is then:

$$\frac{T}{T_e} = 1 + \frac{\gamma - 1}{2}\left[\left(\frac{u_w}{u_e} - 1\right)M\right]^2 r(\eta) +$$
$$\left[\left(\frac{T_w}{T_e} - 1\right) - \frac{\gamma - 1}{2}\left[\left(\frac{u_w}{u_e} - 1\right)M\right]^2 r(0)\right] s(\eta) \tag{A.16}$$

Appendix A. Mirels' Laminar Boundary Layer Approximation

where $r(\eta)$ satisfies

$$r'' + \sigma f r' = \frac{-2\sigma}{\frac{u_w}{u_e} - 1}^2 (f'')^2 \tag{A.17}$$

$$r(\infty) = r'(0) = 0 \tag{A.18}$$

and $s(\eta)$ satisfies

$$s'' + \sigma f s' = 0 \tag{A.19}$$

$$s(0) = 1 \tag{A.20}$$

$$s(\infty) = 0 \tag{A.21}$$

$s(\eta)$ resolves to zero for insulated walls. The relative wall temperature then becomes:

$$\frac{T_{w,i}}{T_e} = 1 + \frac{\gamma - 1}{2} \left[\left(\frac{u_w}{u_e} - 1 \right) M \right]^2 r(0) \tag{A.22}$$

In terms of $T_{w,i}$ the equation becomes

$$\frac{T}{T_e} = 1 + \frac{\gamma - 1}{2} \left[\left(\frac{u_w}{u_e} - 1 \right) M \right]^2 r(\eta) + \left(\frac{T_w}{T_e} - \frac{T_{w,i}}{T_e} \right) s\eta \tag{A.23}$$

$r(0)$ is a recovery factor based on the Mach number of the external flow relative to the wall. Expressing the equations for r and s in quadrature form yields:

$$r = \frac{2\sigma}{\frac{u_w}{u_e} - 1}^2 \int_\eta^\infty [f''(\xi)]^\sigma \, d\xi \int_0^\xi [f''(\theta)]^{2-\sigma} \, d\theta \tag{A.24}$$

$$s = \frac{\int_\eta^\infty [f''(\xi)]^\sigma \, d\xi}{\int_0^\infty [f''(\xi)]^\sigma \, d\xi} \tag{A.25}$$

For Prandtl number $\sigma = 1$

$$r = 1 - \left(\frac{\frac{u_w}{u_e} - f'}{\frac{u_w}{u_e} - 1} \right)^2 \tag{A.26}$$

Appendix A. Mirels' Laminar Boundary Layer Approximation

$$s = \frac{f' - 1}{\dfrac{u_w}{u_e} - 1} \tag{A.27}$$

For x constant, the relationship between y and η is as follows:

$$y\sqrt{\frac{1}{2}\frac{u_e}{x\nu_w}} = \int_0^\eta \frac{T}{T_w} d\eta \tag{A.28}$$

Combining (A.23) yields:

$$y\sqrt{\frac{1}{2}\frac{u_e}{x\nu_w}} = \frac{T_e}{T_w}\left[u + \frac{\gamma - 1}{2}\left[\left(\frac{u_w}{u_e} - 1\right) M\right]^2 \int_0^\eta r\, d\eta + \frac{T_w - T_{w,i}}{T_e}\int_0^\eta s\, d\eta \right] \tag{A.29}$$

Defining the boundary layer to be $\dfrac{u}{u_e} = 0.99$, the laminar boundary layer thickness is

$$\delta = \sqrt{\frac{2}{1 - \dfrac{u}{u_e}}}\sqrt{\frac{\mu_m T}{\mu T_m}}\sqrt{\frac{\nu(u_e\tau - \xi)}{u_e}}$$

$$\left[\frac{2.89\sqrt{1 - \dfrac{u}{u_e}}}{\sqrt{1.413 - \dfrac{u}{u_e}}} + \frac{\gamma - 1}{2}M^2\int_0^\infty r\, d\eta - \left(\frac{T_r}{T_e} - \frac{T_w}{T_e}\right)\int_0^\infty s\, d\eta \right] \tag{A.30}$$

Appendix B

Mirels' Turbulent Boundary Layer Approximation

Mirels' approximation [18] starts with the integral form of the momentum equation,

$$\frac{\tau_w}{\rho_e u_e^2} = \frac{d}{dx} \int_0^\infty \frac{\rho u}{\rho_e u_e} \left(1 - \frac{u}{u_e}\right) dy = \frac{d\theta}{dx} \tag{B.1}$$

where $\dfrac{u}{u_e}$ represents the average velocity. The boundary-layer thickness is defined by $\tilde{\delta}$, and a similarity parameter ζ_T is created to express $\dfrac{u}{u_e}$ as a function of ζ_T. The similarity function is $\zeta_T = \dfrac{y}{\tilde{\delta}}$. Mirels assumed the relationship between the average velocity and the similarity parameter ζ_T was $\dfrac{u}{u_e} = \zeta_T^{\frac{1}{7}}$ based on studies of the turbulent boundary layer on a semi-infinite flat plate.

for $0 \le \zeta_T \le 1$,

$$|\frac{u - u_w}{u_e - u_w}| = \zeta_T^{\frac{1}{7}} \tag{B.2}$$

for $1 \le \zeta_T$

$$|\frac{u - u_w}{u_e - u_w}| = 1 \tag{B.3}$$

Appendix B. Mirels' Turbulent Boundary Layer Approximation

Expressing the relative temperature as a function of density yields for $0 \leq \zeta_T \leq 1$,

$$\frac{\rho_e}{\rho} = \frac{T}{T_e} = \frac{T_w}{T_e} \left(1 + b\zeta_T^{\frac{1}{7}} - c\zeta_T^{\frac{2}{7}}\right) \tag{B.4}$$

for $1 \leq \zeta_T$

$$\frac{\rho_e}{\rho} = \frac{T}{T_e} = 1 \tag{B.5}$$

where

$$b = \frac{T_r}{T_e} - 1 \tag{B.6}$$

$$c = \left(\frac{T_r}{T_e} - 1\right) \frac{T_e}{T_w} \tag{B.7}$$

The boundary-layer momentum thickness and displacement are expressed as

$$\frac{\theta}{\tilde{\delta}} = 7\frac{T_e}{T_w}\left(1 - \frac{u_w}{u_e}\right)\left[\frac{u_w}{u_e}I_6 + \left(1 - 2\frac{u_w}{u_e}\right)I_7 - \left(1 - \frac{u_w}{u_e}\right)I_8\right] \tag{B.8}$$

$$\frac{\delta*}{\tilde{\delta}} = 1 - 7\frac{T_e}{T_w}\left[\frac{u_w}{u_e}I_6 + \left(1 - \frac{u_w}{u_e}\right)I_7\right] \tag{B.9}$$

where $I_6, I_7, and I_8$ are functions of b and c given by

$$I_N = \int_0^1 \frac{z^N dz}{1 + bz - cz^2} \tag{B.10}$$

and $N = 6, 7, or 8$. Assuming constant wall temperature, and knowing $\frac{\theta}{\tilde{\delta}}$ is independent of x, the integral form of the momentum equation becomes

$$\frac{\tau_w}{\rho_e u_e^2} = \frac{\theta}{\tilde{\delta}}\frac{d\tilde{\delta}}{dx} \tag{B.11}$$

The Blasius relation for incompressible flow over a semi-infinite plate is

$$\frac{\tau_w}{\rho_e u_e^2} = 0.0225 \left(\frac{\nu_e}{u_e\tilde{\delta}}\right)^{\frac{1}{4}} \tag{B.12}$$

Appendix B. Mirels' Turbulent Boundary Layer Approximation

Evaluating the fluid properties at a mean temperature allows for expansion of the Blasius relation to compressible flow.

$$\frac{\tau_w}{\rho_e u_e^2} = 0.0225\phi \left(\frac{\nu_e}{u_e \tilde{\delta}}\right)^{\frac{1}{4}} \tag{B.13}$$

where ϕ is defined as

$$\phi = \left(\frac{\mu_m}{m_e}\right)^{\frac{1}{4}} \left(\frac{T_m}{T_e}\right)^{\frac{3}{4}} \tag{B.14}$$

Mirels found a reasonable estimate for the mean temperature to be

$$T_m = 0.5(T_w + T_e) + 0.22(T_r - T_e) \tag{B.15}$$

For a moving reference frame, where the wall is in motion, the relative velocity is imposed on the compressible flow expression, resulting in

$$\frac{\tau_w}{\rho_e u_e^2} = 0.0225\phi \left(1 - \frac{u_w}{u_e}\right) |1 - \frac{u_w}{u_e}|^{\frac{3}{4}} \left(\frac{\nu_e}{u_e \tilde{\delta}}\right)^{\frac{1}{4}} \tag{B.16}$$

Substituting (B.16) into (B.11) allows for integration. For a constant T_w with adiabatic conditions, the boundary layer thickness is found to be

$$\tilde{\delta} = 0.0574 \left(\phi \frac{1 - \frac{u_w}{u_e}}{\frac{\theta}{\tilde{\delta}}}\right)^{\frac{4}{5}} |1 - \frac{u_w}{u_e}|^{\frac{3}{5}} \left(\frac{\nu_e}{u_e x}\right)^{\frac{1}{4}} x \tag{B.17}$$

References

[1] R.D. Zucker and O. Biblarz. *Fundamentals of Gas Dynamics*. John Wiley and Sons, Hoboken, NJ, second edition, 2002.

[2] J. E. John and T.G. Keith. *Gas Dynamics*. Prentice Hall, Upper Saddle River, NJ, 2006.

[3] The Physics Hypertexbook. Shock Waves, Online; accessed 21-January-2014. http://physics.info/shock/.

[4] G.F. Kinney and K.J.E. Graham. *Explosive Shocks in Air*. Springer-Verlag, New York, NY, 1985.

[5] G. Ben-Dor. *Shock Wave Reflection Phenomena*. Springer-Verlag, New York, NY, 1997.

[6] E. Loth and L. Povinelli. Canonical normal shock wave/boundary-layer interaction flows relevant to external compression inlets. *AIAA Journal*, 51(9):2208–2217, September 2013.

[7] H. Babinsky and J.K. Harvey. *Shock Wave-Boundary-Layer Interactions*. Cambridge University Press, New York, NY, 2011.

[8] R. Brun, P. Auberger, and N. Van Que. Shock tube study of boundary layer instability. *Acta Astronautica*, 5:1145–1152, 1978.

[9] A. Weiss and H. Olivier. Behaviour of a shock train under the influence of boundary-layer suction by a normal slot. *Experiments in Fluids*, 52:273–287, 2012.

[10] J.A. Schetz and R.D.W. Bowersox. *Boundary Layer Analysis*. AIAA, Reston, VA, second edition, 2011.

References

[11] B.R. Munson, D.F. Young, T.H. Okiishi, and W.W. Huebsch. *Fundamentals of Fluid Mechanics.* John Wiley and Sons, Hoboken, NJ, sixth edition, 2008.

[12] The Free Dictionary. Boundary-layer Flow, Online Source, accessed 23-January-2014. http://encyclopedia2.thefreedictionary.com/boundary-layer+flow.

[13] S. Elghobashi. On predicting particle-laden turbulent flows. *Applied Scientific Research*, 52(4):309–329, 1994.

[14] W.J. Chyu, M.J. Rimlinger, and T.I-P. Shih. Control of shock-wave/boundary-layer interactions by bleed. *AIAA Journal*, 33(7):1239–1247, July 1995.

[15] M.J. Anderson. *Oblique Shock Interactions with Perturbed Density Interfaces.* PhD thesis, University of New Mexico, 2011.

[16] R.L. White. Oblique shock wave interactions with gas cylinder interfaces. Master's thesis, University of New Mexico, 2012.

[17] D. Olmstead, P. Wayne, J. Vigil, T. Bernard, C.R. Truman, and P. Vorobieff. Blast Born Vortices. 2013. http://www.aps.org/units/dfd/pressroom/gallery/2013/vorobieff.cfm.

[18] H. Mirels. Boundary Layer Behind Shock or Thin Expansion Wave Moving into Stationary Fluid TN-3712. Technical report, National Advisory Committee for Aeronautics, 1955.

[19] E.L. Petersen and R.K. Hanson. Improved turbulent boundary-layer model for shock tubes. *AIAA Journal*, 41(7):1314–1322, 2003.

[20] R.J. Emrich and D.B. Wheeler Jr. Wall effects in shock tube flow. *Physics of Fluids*, 1(1):14–23, 1958.

[21] E.J. Gion. Measured velocity profiles in the laminar boundary layer behind a shock. *Physics of Fluids*, 8(3):546–547, 1965.

[22] N.J. Fox, T.I. McLaren, and R.M. Hobson. Test time and particle paths in low-pressure shock tubes. *Physics of Fluids*, 9(12):2345–2350, 1966.

[23] E.W. Hubbard and P.C.T. de Boer. Flow field behind a shock wave in a low-pressure test gas. *Physics of Fluids*, 12(12):2515–2521, 1969.

[24] H. Mirels. Attenuation in a Shock Tube due to Unsteady-Boundary-Layer Action Report 1333. Technical report, National Advisory Committee for Aeronautics, 1957.

References

[25] H. Mirels. Shock tube test time limitation due to turbulent-wall boundary layer. *AIAA Journal*, 2(1):84–93, 1964.

[26] H. Mirels. Flow nonuniformity in shock tubes operating at maximum test times. *Physics of Fluids*, 9(10):1907–1912, 1966.

[27] H. Mirels. Turbulent boundary layer behind constant velocity shock including wall blowing effects. *AIAA Journal*, 22(8):1042–1047, 1984.

[28] V.M. Boiko, S.P. Kiselev, A.N. Papyrin, S.V. Poplavsky, and V.M. Fomin. Shock wave interaction with a cloud of particles. *Shock Waves*, 7:275–285, 1997.

[29] T. Suzuki, Y. Sakamura, O. Igra, T. Adachi, S. Kobayashi, A. Kotani, and Y. Funawatashi. Shock tube study of particles' motion behind a planar shock wave. *Measurement Science and Technology*, 16:2431–2436, October 2005.

[30] J.L. Wagner, S.J. Beresh, S.P. Kearney, B.O. Pruett, and E.K. Wright. Shock tube investigation of quasi-steady drag in shock-particle interactions. *Physics of Fluids*, 24(12):123301, 2012.

[31] E. Loth. Compressibility and rarefaction effects on drag of a spherical particle. *AIAA Journal*, 46(9):2219–2228, 2008.

[32] M. Parmar, A. Haselbacher, and S. Balachandar. Improved drag correlation for spheres and application to shock-tube. *AIAA Journal*, 48(6):1273–1276, 2010.

[33] R.J. Goldstein, editor. *Fluid Mechanics Measurements*. Taylor and Francis, Washington, D.C., second edition, 1996.

[34] H.Z. Cummins, N. Knable, and Y. Yeh. Observation of Diffusion Broadening of Rayleigh Scattered Light. *Physical Review Letters*, 12:150–153, 1964.

[35] J. Westerweel. Fundamentals of digital particle image velocimetry. *Measurement Science and Technology*, 8:1379–1392, 1997.

[36] S.J. Lee, M.K. Chung, C.W. Mun, and Z.H. Cho. Experimental Study of Thermally Stratified and Unsteady Flow by NMR-CT. *Experiments in Fluids*, 5:273–281, 1987.

[37] LaVision GmbH, Gottingen, Germany. *DaVis 8.1 Software Product Manual*, September 2013.

[38] H. Mirels. Laminar Boundary Layer Behind Shock Advancing into Stationary Fluid TN-3401. Technical report, National Advisory Committee for Aeronautics, 1955.